AIAA AVIATION Forum
June 15-19, 2020, VIRTUAL EVENT
AIAA AVIATION 2020 FORUM

10.2514/6.2020-2996



# Numerical Study of Hypersonic Boundary Layer Receptivity over a Blunt Cone to Freestream Pulse Disturbances

Simon He* and Xiaolin Zhong†
*University of California, Los Angeles, California, 90095, USA*

**While receptivity plays a key role in the transition of hypersonic flows, most prior computational receptivity studies have neglected to replicate realistic broadband and continuous frequency disturbance spectra. This work uses perfect gas Linear Stability Theory (LST) and Direct Numerical Simulation (DNS) to study the receptivity of flow over a 9.525 mm nose radius, 7-degree half-angle straight cone at Mach 10 using finite spherical and planar pulses to approximate disturbances with continuous and broadband frequency spectra. Freestream fast acoustic, slow acoustic, temperature, and vorticity pulses of both geometries were studied to investigate a wide range of forcing conditions. Unsteady DNS predicts second mode growth and agrees well with LST. DNS and LST data are used to extract second mode receptivity coefficients and phase spectra. For the finite pulses the strongest to weakest responses are for the fast acoustic, temperature, slow acoustic, and vorticity pulses respectively. The planar disturbances show the strongest response for the slow acoustic, temperature, vorticity, and fast acoustic pulses in that order. FFT results vary strongly in noise dependency based on the disturbance type and pulse geometry, and the planar fast acoustic case in particular is shown to be much more receptive to forcing modes.**



## I. Introduction

The accurate prediction of laminar to turbulent transition in hypersonic flows is a major concern when using computational fluid dynamics (CFD) to aid in the design of high-speed vehicles. Transition to turbulence is known both to dramatically increase aerodynamic drag and heating on the vehicle's surface and to significantly affect the control of the vehicle [1–3]. Delaying transition and accurately predicting transitioanry behavior in hypersonic flows will allow for greater specificity in the design of thermal protection systems (TPS). Doing so would have a substantial payoff, potentially improving flight performance and expanding payload capacities for future hypersonic vehicles.

Transition in a hypersonic boundary layer is governed by several mechanisms, and in the case of weak environmental forcing can be broken down into three distinct stages: (i) boundary layer receptivity, (ii) linear growth of small amplitude disturbances, and (iii) nonlinear breakdown at finite disturbance amplitudes [4]. Traditionally, studies on hypersonic boundary layer transition at zero angle of attack have focused on the linear growth of Mack modes, for which the second mode instability has been found to dominate [5]. Receptivity mechanisms dictate the initial disturbance amplitudes of flow instabilities, such as the second mode, in response to external forcing. These initial amplitudes can greatly impact the general stability behavior of the flow[6]. Studies of receptivity commonly focus on the response to freestream noise which, for compressible flows, can be categorized into three distinct types: acoustic, entropy, and vorticity disturbances[7]. A schematic of the various receptivity processes is presented in Fig. 1. In hypersonic flows, the interaction of freestream disturbances of any of these categories with the bow shock generates disturbance waves of all three types that can perturb the boundary layer[8]. However, the differing shock interaction mechanisms between these initial freestream disturbance types can cause significant differences in the resulting boundary layer disturbance content, both in terms of wave amplitude and phase[9]. Thus, a wide-ranging consideration of all the disturbance types with realistic continuous frequency spectra is needed to fully characterize the receptivity of a hypersonic flow.

The receptivity of hypersonic boundary layers to freestream disturbances has been extensively studied in several geometries, with work on flat plates being especially substantial[4, 10–15]. In their theoretical study, Balakumar and Malik[10] found that point source disturbances generated complex disturbance profiles consisting of both continuous and discrete modes in the boundary layer. Ma and Zhong [4, 11, 12] confirmed this in their computational studies and also found that freestream acoustic disturbances generate initially stable modes near the leading edge of their flat plate, which then become unstable after synchronization. Synchronization occurs when the discrete modes (described by Mack

*Ph.D. Student, Mechanical and Aerospace Engineering Department, simon.he.ucla@gmail.com, AIAA Student Member.
†Professor, Mechanical and Aerospace Engineering Department, xiaolin@seas.ucla.edu, AIAA Associate Fellow.

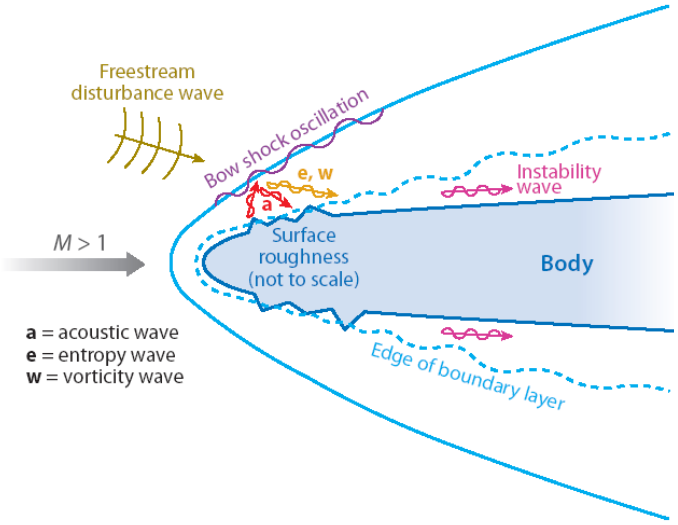


**Fig. 1 Schematic of general receptivity mechanisms, adapted from[3].**

as the multiple-viscous solutions[16]) originating from the continuous freestream fast and slow acoustic spectra interact and exchange energy. This exchange can eventually destabilize one of the discrete modes and cause an amplifying Mack mode instability. In their studies, Ma and Zhong[4] found that freestream acoustic, vorticity, and entropy waves modelled as discrete frequency Fourier modes could all excite discrete mode disturbances in flat plate boundary layers, though the receptivity mechanisms differed greatly between the disturbance types. They showed that a freestream entropy disturbance excited strong stable mode I (F1) disturbances upstream on the plate that would then be converted into stable mode II (F2) mode instabilities after synchronization. The freestream fast acoustic disturbance similarly excited stable mode I (F1) and mode II (F2) disturbances. However, stronger oscillations which were indicative of much more substantial multimodal coupling were observed for the fast acoustic case. The slow acoustic disturbance was instead shown to successfully excite an unstable second mode, which was found to be what is now known as the discrete mode S, downstream of synchronization. Malik and Balakumar[13] similarly found that planar, discrete frequency slow acoustic waves impinging on a flat plate generated much stronger receptivity responses compared to other disturbances and that leading-edge bluntness seemed to stabilize the boundary layer. Fedorov et al.'s[15] flat plate receptivity study focused on the response to a temperature disturbance imposed either upstream of or downstream of the shock. When the temperature disturbance was imposed directly on the boundary layer they found that a discrete mode F was generated. After experiencing intermodal exchange, these initial mode F disturbances excited the unstable mode S. Similarly for the freestream disturbance case, Fedorov et al. found that significant acoustic waves were excited behind the shock after interaction. These then propagated into and through the boundary layer to also excite the unstable mode S disturbance. This shock-disturbance interaction generated perturbation amplitudes that were an order of magnitude higher than those associated with the pure boundary layer disturbance and reflected a strong receptivity mechanism directly linked to shock interactions. The mode F and mode S terminology discussed here were recently coined by Fedorov and Tumin to more directly reflect the asymptotic behavior of the discrete modes, and is discussed in detail in[17]. The results of these studies indicate diffierent receptivity paths for different disturbance types, and necessitate a wide-ranging consideration of disturbances in order to fully characterize the receptivity response of a flow.

Numerous studies have also been made on the receptivity of cone geometries to freestream disturbances[18–23]. Zhong and Ma[18] investigated the receptivity of a blunt cone with discrete frequency freestream fast acoustic waves at Mach 7.99. They found through LST that the unstable second mode for this case was mode S, similar to their previous flat plate case [4]. Contrary to their previous flat plate result, the fast acoustic disturbance was also found to excite the second mode instability in the boundary layer for the cone. This indicated that the receptivity process differed significantly between these two geometries, which can be attributed to flow features such as bow shock interactions, nose bluntness, and potential entropy layer instabilities. Similarly, Balakumar and Kegerise [19, 20] found that both discrete frequency vorticity and acoustic disturbances could similarly excite second mode instabilities in cone flows, and that the receptivity response was stronger for acoustic disturbance waves. They also reported that wave incidence

had some effect on the receptivity response, indicating a need to account for more complex disturbance conditions to fully approximate the envelope of conditions found in flight. Kara et al.[22] used receptivity simulations for discrete frequency acoustic waves to predict transition on sharp and blunt cones. They found that while freestream acoustic waves readily generated second mode instabilities downstream on the cone, second mode amplification was unable to accurately predict the transition behavior observed in large nose bluntness cones. Possible explanations for this include non-modal disturbance growth from sources like transient growth[24], or a failure to accurately capture the effects of freestream environmental noise in the disturbance model[25].

Past receptivity studies utilized planar freestream disturbances modelled as discrete frequency Fourier modes[4, 20]. However, this fails to account for the broadband frequency distribution of freestream noise present in both experimental and true flight conditions[6]. Balakumar and Chou[21] approximated these broadband frequency disturbances through carefully chosen combinations of discrete frequency, two-dimensional planar slow acoustic waves which were imposed simultaneously on the flow. The amplitude of each disturbance wave in the packet was determined by equating the energy of each discrete wave with a chosen frequency bin in the experimentally measured freestream noise spectrum. Through this method they were able to calculate second mode receptivity coefficients, defined as the normalized surface pressure disturbance at the neutral point, for a variety of sharp and blunt cone cases. They found that receptivity coefficients decreased with nose bluntness and that the new receptivity data allowed for fairly accurate transition prediction for their sharp nose cases using a surface pressure threshold criterion. However, the accuracy of the threshold criterion they used decreased significantly for blunter cones.

Huang and Zhong [9, 26] instead modeled a broadband disturbance through the use of a finite axisymmetric freestream hotspot, which was equivalent to an entropy disturbance, over a compression cone. They showed that this hotspot was effective in exciting second mode instabilities in the boundary layer. They also found that the resulting disturbance growth rate and phase speed compared well to LST, and corroborated the results from the experimental studies at Purdue by Wheaton et al.[27] and Chou et al.[28, 29] that the simulations were based on. The receptivity mechanism for the entropy spot over a compression cone was found to be very similar to that of discrete acoustic waves over a blunt cone, but different from entropy spot disturbances for flat plates. This further reinforces the significance of geometry for receptivity mechanisms. They were then able to use a combination of the unsteady DNS and the LST disturbance data to extract both spectral receptivity coefficients for the second mode, and the phase angle spectra of the boundary layer disturbance. With these results, the full response to this particular temperature disturbance as well as other arbitrary axisymmetric temperature disturbances can be reconstructed[9, 23]. While these studies showed that Gaussian pulses could successfully approximate continuous frequency spectrum disturbances and excite significant modal instabilities in hypersonic flows over cones, they were very limited in terms of the disturbances that were considered. Additional acoustic and vorticity disturbances must also be investigated to account for the differences in receptivity mechanisms between disturbance types.

The most direct application of receptivity data is in the development of improved transition estimation methods. LST has historically been used to track the spatial and temporal development of discrete instability modes, though parabolized stability equations (PSE) have also risen in prominence recently to account for nonparallel and nonlinear effects[30]. Current transition prediction procedures, such as the $e^N$ method, rely on using modal instability growth rates derived from LST or PSE to determine the relative amplification of boundary layer disturbances. Empirically determined threshold values are then used to predict the onset of turbulent transition[21, 31, 32]. This prediction approach assumes that relative amplification is the most critical factor in determining transition and often ignores the initial disturbance amplitudes generated by receptivity. While this assumption can provide good internal consistency in a given experimental environment, transition thresholds based on this methodology can vary significantly between different experiments. Schneider[6] described similar experiments with threshold N-factors of 5 and 8, demonstrating the potential impact of environmental noise on transition. Variability of this degree prevents the widespread application of uncorrected prediction results between experiments.

A number of improved transition prediction methodologies have been proposed to overcome the limitations of the traditional $e^N$ method. Crouch[31] proposed a variable N-factor method that corrects the traditional $e^N$ method through fitting a variation of the N-factor with a simplified model of the freestream response. This has the advantage of requiring no additional computations after the disturbance response and linear growth (N-factor) data are first obtained. Another improved transition model is based on the amplitude method proposed by Mack[33], which also uses experimental receptivity data to correlate initial disturbance amplitudes to freestream noise environments. Marineau[34] used this amplitude method, empirical receptivity correlations, and simulation results in an iterative process to estimate transition on a selection of sharp and blunt nosed cones. He showed that this method could predict transition for blunt cones and cones at angles of attack much more accurately than more traditional $e^N$ methods. Ustinov[35] also extended this

amplitude method to investigate laminar-turbulent transition on a swept wing using a combined amplitude criterion for steady state and time dependent perturbations in the flow and found that this method successfully reproduced experimentally observed dependencies on Reynolds number, local surface roughness, and freestream turbulence. The receptivity results applied in Crouch's and Marineau's studies were based on highly empirical correlations. Utilizing receptivity spectra derived from DNS simulations would provide significantly improved precision and potentially help further improve the accuracy of these alternative transition prediction methods.

The current study presents a novel consideration of multiple pulses varying in both type and geometry in order to generate a more complete view of the receptivity response of cones to continuous, broadband frequency freestream pulse disturbances. Previous computational receptivity studies of similar geometries have focused primarily on less realistic discrete frequency disturbances, or very specifically on broadband temperature disturbances. While these works provide insight into the complex receptivity mechanisms present in hypersonic flow over blunt cones, a more complete overview of the disturbance response is necessary to fully characterize the receptivity mechanisms for the more realistic broadband frequency disturbances present in both experimental and flight conditions. The receptivity mechanisms for both finite, spherical and planar pulse geometries are studied in order to investigate the effects of continuous forcing on the stability of the cone. Fast acoustic, slow acoustic, temperature, and vorticity disturbances are modelled using both of the pulse geometries for a total of eight unsteady cases. The meanflow geometry is based on experiments by Marineau et al.[36] for a Mach 10 flow over a cone from the AEDC windtunnel 9. The numerical study in this paper consists of three primary components: (1) the steady meanflow simulation and LST analysis, (2) the unsteady DNS simulation using the freestream pulse disturbances, and (3) the generation of the spectral receptivity coefficients and phase angles using the LST and unsteady DNS results.



## II. Simulation Conditions

This study aims to expand on previous work by Huang and Zhong[9, 26] which detailed the receptivity response of flow over a flared cone at Mach 6 to freestream temperature pulses, and used a combination of LST and unsteady DNS to generate receptivity coefficients. The current study focuses on the receptivity of a 9.525 mm nose radius circular, straight cone with a half-angle of 7 degrees at mach 10 to freestream finite spherical fast acoustic, slow acoustic, temperature, and vorticity disturbances as well as freestream planar fast acoustic, slow acoustic, temperature, and vorticity disturbances. The perturbations were modelled as Gaussian pulses in the freestream, providing for continuous, broadband frequency disturbances. The cone geometry is 1.9 m in length. The DNS simulations used 240 points in the wall-normal direction and roughly five points per millimeter on the surface of the cone in the streamwise direction. Four points are used in the periodic spanwise direction, though only one point is directly calculated at each timestep. The flow conditions for this study are summarized in Table 1 and are based on the tunnel conditions reported by Marineau[36] for run 3752.

**Table 1 Freestream flow conditions for DNS simulations.**

| Parameter | Value | Parameter | Value |
|---|---|---|---|
| $M_\infty$ | 9.79 | $h_{0,\infty}$ | 1.07 MJ/kg |
| $\rho_\infty$ | 0.0427 kg/m$^3$ | $p_\infty$ | 0.65 kPa |
| $T_\infty$ | 51.0 K | $U_\infty$ | 1426 m/s |
| $T_w/T_{0,\infty}$ | 0.3 | $Pr$ | 0.72 |
| $Re/m \quad (1E6/m)$ | 18.95 | *Angle of Attack* | 0° |

The DNS code used in this study utilizes a shock-fitting formulation with the parameters in Table 1 defining the freestream conditions upstream of the shock formed over the body. Marineau et al.[36] used curve fits of experimental data to generate the viscosity used for the Reynolds number calculations instead of Sutherland's Law. This leads to approximately a 15% difference in the calculated freestream unit Reynolds numbers between this study and Marineau's.

## III. Governing Equations

The receptivity simulations in this study assume perfect gas behavior for molecular nitrogen in the flow field. This assumption was made based on the low freestream stagnation enthalpy reported in Table 1. The three-dimensional

conservative Navier-Stokes system consists of a single species mass conservation equation, three momentum conservation equations, and the energy equation. The governing equations in vector form are written as

$$\frac{\partial U}{\partial t} + \frac{\partial F_j}{\partial x_j} + \frac{\partial G_j}{\partial x_j} = 0, \quad (j = 1, 2, 3) \tag{1}$$

where $U$ is the state vector of conserved quantities and $F_j$ and $G_j$ are the inviscid and viscous flux vectors, respectively. Here, the j indices indicate Cartesian coordinates in the streamwise, radial, and azimuthal directions about the cone. The conservative vector $U$ is comprised of five conservative flow variables for mass, momentum, and energy. For further details of the governing equations for the study, refer to the previous work by Zhong[37].

## IV. Numerical Methods and Disturbance Model

### A. DNS

The DNS code utilizes a high-order shock-fitting method for a perfect gas flow that was developed to compute the flow field between the shock and the body. The numerical method is summarized here for clarity. For shock-fitting computations the shock location is treated as an additional unknown and is solved along with the flow field. Since the shock position is not stationary, the grid used to compute the flow field is a function of time. First, the Navier-Stokes equations are transformed into computational space

$$\frac{1}{J}\frac{\partial U}{\partial \tau} + \frac{\partial E'}{\partial \xi} + \frac{\partial F'}{\partial \eta} + \frac{\partial G'}{\partial \zeta} + \frac{\partial E'_v}{\partial \xi} + \frac{\partial F'_v}{\partial \eta} + \frac{\partial G'_v}{\partial \zeta} + U\frac{\partial (1/J)}{\partial \tau} = 0 \tag{2}$$

where $J$ is the Jacobian of the coordinate transformation and $(\xi, \eta, \zeta)$ are the transformed computational coordinates in the streamwise, radial, and azimuthal directions of the cone. A low-dissipation, fifth-order upwinded stencil is used for the inviscid fluxes, a sixth-order central stencil is used to discretize the viscous terms, and the shock itself is treated as a computational boundary. The flow variables after the shock are determined through a combination of the Rankine-Hugoniot relations across the shock and a characteristic compatibility relation behind the shock. Finally, the solution is advanced in time using a low-storage first-order Runge-Kutta method from Williamson[38]. The details of this shock-fitting formulation and the numerical methods can be found in Zhong[37].

### B. LST

The Linear Stability Theory (LST) implementation used in this study was originally developed and verified by Ma and Zhong [4, 11, 12]. The LST relations are derived from the governing Navier-Stokes equations in Eq. 1 where the instantaneous flow can be decomposed into a mean and fluctuating component $q = \overline{q} + q'$. This instantaneous flow is then reintroduced into the governing equations. Since the steady mean flow component is assumed to satisfy the governing equations, it can be subtracted out. The mean flow is assumed to be quasi-parallel and thus any remaining mean flow terms are functions of $y$ only. Disturbances are also assumed to be small enough that quadratic and higher order perturbation terms can be ignored, allowing for the linearization of the equations. A normal mode solution in the form of $q' = \hat{q}(y) \exp\left[i\left(\alpha x + \beta z - \omega t\right)\right]$ is introduced, where $\omega$ is the circular frequency of the disturbance and $\alpha$ and $\beta$ are the wavenumbers. In this study a spatial stability approach is used. Thus $\alpha$ is complex and results in the dispersion relation $\alpha = \Omega(\omega, \beta)$. For the spatial stability approach, the circular frequency of a disturbance mode, $\omega$, must be manually set to be a real number while $\beta$ is set to 0 for a two dimensional disturbance. The chosen $\omega$ is based on the disturbance frequency being studied and the complex spatial wavenumber $\alpha$ that is solved for can be written as $\alpha = \alpha_r + i\alpha_i$. Here, $-\alpha_i$ is the growth rate of the disturbance. Substituting in the normal mode reduces the problem to a coupled set of 5 ordinary differential equations

$$\left(\mathbf{A}\frac{d^2}{dy^2} + \mathbf{B}\frac{d}{dy} + \mathbf{C}\right)\vec{\phi} = \vec{0}. \tag{3}$$

where $\vec{\phi} = \left[\hat{u}, \hat{v}, \hat{P}, \hat{T}, \hat{w}\right]^T$ and $\mathbf{A}$, $\mathbf{B}$ and $\mathbf{C}$ are complex square matrices of size 5. This is now a boundary value problem where the derivative operators can be discretized and the equations solved numerically. The system of equations is solved using using a multi-domain spectral method similar to Malik[39].

**Table 2 Gaussian pulse parameters for DNS.**

| Pulse Geometry | $\epsilon$ | $\sigma$ | $x_0$ |
|---|---|---|---|
| Finite Spherical | $5E-4$ | $1E-3$ | $-0.02m$ |
| Planar | $1E-6$ | $1E-3$ | $-0.02m$ |

While LST can be used to identify both the unstable disturbance frequencies and their growth rates, it does not directly specify the exact amplitude of the disturbance. Conventionally, boundary-layer transition is estimated using LST through an amplification criterion known as the $e^N$ or the N-factor method. The N-factor is given by:

$$e^{N(s^*,f)} = \frac{A(s^*,f)}{A_0(f)} = \exp\left[\int_{s_0^*}^{s^*} -\alpha_i(s^*,f)ds^*\right] \tag{4}$$

Here $A(s^*,f)$ is the integrated disturbance amplitude, $A_0(f)$ is the initial disturbance amplitude, $s_0^*$ is the location where the disturbance first becomes unstable at the branch I neutral point, and $\alpha_i$ is the spatial amplificatifon rate obtained from LST. The integration is performed for a constant frequency $f$, and is done numerically using trapezoidal integration. Note that a negative imaginary the wave number $\alpha$ results in disturbance growth while a positive value results in disturbance decay. The N-factor is specifically the exponent of $e^N$. In-flight transition N-factors are commonly understood to be between 5 and 10. However, this transition N-factor seems to hold only for sharp cones. Lei [25], Aleksandrova et al.[40], and Balakumar and Chou[21] found that N-factors decreased considerably at similar streamwise locations for blunter cones. Marineau et al. [36] also found that blunt nose N-factors calculated at the beginning of transition were significantly lower than those for sharp nose cases, reaching as low as 0.5. Pure considerations of the N-factor are observed to be insufficient to reliably determine transition throughout a wide variety of conditions.

### C. Freestream Disturbance Model

The stability of the system is also studied by perturbing the meanflow and tracking the development of the resulting disturbances using DNS. Here, the flow is perturbed with freestream fast acoustic, slow acoustic, temperature, and vorticity disturbances in the form of Gaussian pulses. Finite spherical and planar pulse geometries were studied utilized in this work. Since the shock is treated as a computational boundary in the simulations, these pulses can be represented analytically in the freestream. The design of the pulses are based on previous work by Huang and Zhong[9] and Lei and Zhong[23]. We first begin with the temperature disturbance given in Eq. 5.

$$T(x,y,z,t) = \epsilon\, T_\infty exp\left(-\frac{R_c^2}{2\sigma^2}\right) + T_\infty. \tag{5}$$

where the Gaussian parameters are given in Table 2. Additionally, for a perfect gas the equation of state can be used to derive the equivalent freestream density/entropy perturbation.

$$\rho(x,y,z,t) = \frac{p_\infty}{RT(x,y,z,t)} \tag{6}$$

In Eq. 5 $\epsilon T_\infty$ refers to the maximum freestream temperature perturbation amplitude. This amplitude was chosen to ensure that disturbances remained small enough to be applicable to remain in the linear growth regime[4, 9]. The term $\sigma$ controls the width of the pulse and also determines the frequency content of the disturbance while $R_c$ refers to the radial distance from the center of the temperature pulse to a point $(x,y,z)$ in the flow field. For a finite spherical pulse $R_c$ is defined in Eq. 7, while for a planar temperature pulse $R_c = x - x_{pulse}$. The pulse width parameter $\sigma$ was chosen to encompass significant freestream disturbances at frequencies up to 600 kHz in order to study the effects of extensive noise on the flow. This resulted in a pulse radius of approximately 3 mm.

$$R_c = \sqrt{(x-x_{pulse})^2 + (y-y_{pulse})^2 + (z-z_{pulse})^2} \tag{7}$$

In Eq. 7 the coordinates $(x_{pulse}, y_{pulse}, z_{pulse})$ correspond to the center of the pulse. It is assumed that the disturbance propagates purely in the streamwise direction along the central axis of symmetry such that $y_{pulse} = z_{pulse} = 0$ and

$x_{pulse} = x_0 + U_\infty t$ where $x_0$ is the initial location of the temperature in the unsteady simulation and $U_\infty$ is the freestream velocity. The other disturbances are also assumed to propagate in this manner.

The parameters given in Table 2 for the finite spherical cases result in the disturbance distribution shown in Fig. 2 and can be tuned accordingly to generate different spectral amplitude distributions. The frequency distribution of the planar disturbances follow the same trends as the finite spherical cases, with the only difference being in the reduction of the peak disturbance amplitude. The amplitude of the planar disturbances was reduced to ensure that the downstream perturbations remained linear, as the planar disturbances continuously introduce additional forcing waves into the flow throughout the domain.

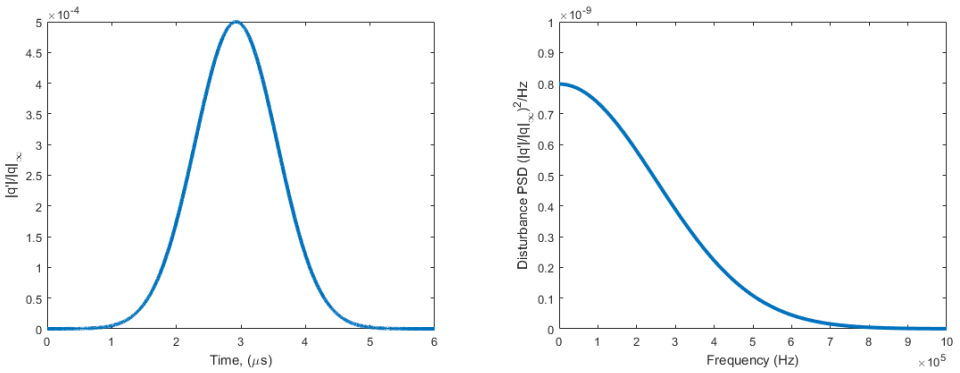


(a) (b)

**Fig. 2 Freestream disturbance distributed over (a) time and (b) frequency for axisymmetric pulse.**

The acoustic freestream disturbances were also modelled using the same Gaussian model. A finite spherical gaussian disturbance for the acoustic and vorticity disturbances assumes an amplitude distribution in the form of Eq. 8.

$$q(x, y, z, t) = |q'|_\infty exp\left(-\frac{(R_c)^2}{2\sigma^2}\right) + q_\infty \tag{8}$$

For acoustic and vorticity disturbances, the coefficient q corresponds to any perturbation variable in the freestream. Additionally, q' represents the peak perturbation amplitude of each of these variables normalized by the freestream value. In the case of a fast acoustic disturbance, the freestream disturbance amplitudes follow the dispersion relations given by[41]:

$$|\rho'|_\infty = \frac{|P'|_\infty}{\gamma} = |u'|_\infty M_\infty = \epsilon M_\infty, \quad |s'|_\infty = |v'|_\infty = |w'|_\infty = 0 \tag{9}$$

A slow acoustic disturbance in the freestream is governed by a very similar dispersion relation:

$$|\rho'|_\infty = \frac{|P'|_\infty}{\gamma} = -|u'|_\infty M_\infty = \epsilon M_\infty, \quad |s'|_\infty = |v'|_\infty = |w'|_\infty = 0 \tag{10}$$

And a freestream vorticity disturbance is described by:

$$|v'|_\infty M_\infty = \epsilon M_\infty, \quad |u'|_\infty = |p'|_\infty = |s'|_\infty = 0 \tag{11}$$

Furthermore, these disturbances propagate in the freestream at a phase speed of $C_\infty$, which is defined as $C_\infty = U_\infty + a_\infty$ for fast acoustic disturbances, $C_\infty = U_\infty - a_\infty$ for slow acoustic disturbances, and $C_\infty = U_\infty$ for entropy/vorticity disturbances. Here $U_\infty$ is the freestream velocity and $a_\infty$ is the speed of sound in the freestream. In order to ensure that the same frequency spectra is shared among the disturbances, the pulse width term $\sigma$ must be scaled by $1 + 1/M_\infty$ for a fast acoustic disturbance and by $1 - 1/M_\infty$ for a slow acoustic disturbance.

A planar pulse is defined in a similar manner in Eq. 12 for the acoustic and vorticity disturbances where the only difference is that $R_c$ has been replaced with a simplified pulse distribution purely in x.

$$q(x, y, z, t) = |q'|_\infty exp\left(-\frac{(x - x_{pulse})^2}{2\sigma^2}\right) + q_\infty \tag{12}$$

The disturbances in each of these cases is modelled to propagate through the freestream through the term $x_{pulse}$ defined in Eq. 13.

$$x_{pulse} = x_0 + C_\infty t \tag{13}$$

### D. Boundary Layer Receptivity

The pulse disturbances imposed onto the cone in the unsteady simulations were chosen to induce broadband frequency perturbations in the boundary layer of the cone. In order to study the evolution of discrete frequency disturbances and correlate the unsteady DNS results with LST, the unsteady DNS is decomposed into its constituent frequency components. This was done using Fourier spectral analysis.

The time-dependent perturbation variables can be expressed in terms of their Fourier spectral components, obtained through a Fast Fourier Transform (FFT):

$$h(t_k) \equiv h_k \approx \sum_{n=0}^{N-1} H(f_n) e^{-2\pi i f_n t_k} \tag{14}$$

where $H(f_n)$ is the frequency space Fourier coefficient corresponding to the $n$th discretized frequency $f_n$ . Additionally, N corresponds to the total number of Fourier collocation points used to discretize the time-dependent function $h(t)$ in Fourier space. The discretized time function $h_k$ is defined as being the value of the time dependent function $h(t)$ at a given time $t = t_k$.

In this study, the variable $h(t)$ corresponds to local boundary-layer perturbations in the surface pressure, though other flow variables such as temperature and density may also be considered. The complex Fourier coefficients $H(f_n)$ correspond to the phase angle of the perturbation variables, and $|H(f_n)|$ are the perturbation amplitudes for these variables at a given frequency.

Since LST was used to validate the results of the unsteady DNS analysis, local growth rates and wavenumbers need to be calculated from the Fourier decomposed perturbation data. Following a similar procedure to Ma and Zhong[4] and Huang and Zhong[9], the local growth rates for each frequency are determined by

$$-\alpha_i = \frac{1}{|H(f_n)|} \frac{d|H(f_n)|}{ds} \tag{15}$$

and the local wave numbers are determined by

$$\alpha_r = \frac{d\phi_n}{ds} \tag{16}$$

where $s$ corresponds to the local streamwise coordinates, $f_n$ is the $n$th disturbance frequency of interest, and $\phi_n$ is the disturbance phase angle of the $n$th frequency. The phase speed of a given disturbance at a given frequency is defined as

$$c_r = \frac{2\pi f_n}{\alpha_r} \tag{17}$$

The response of the system to each freestream disturbance environment is can be represented through a receptivity coefficient. This receptivity coefficient $C_{rec}(f)$, defined here as the initial amplitude of the second mode disturbance at the branch I neutral point for a discrete frequency $f$ to freestream forcing of the same frequency, is determined using a combination of LST and unsteady DNS data. In the presence of a strong second mode it is assumed that the receptivity coefficient can be extracted by inverting the amplification factor (N-factor) relation, as shown in Eq. 18.

$$C_{rec}(f) = A_0(f) = \frac{A(s^*, f)}{e^{N(s^*, f)}} \tag{18}$$

Here $A(s^*, f)$ is the Fourier decomposed surface pressure normalized by the freestream disturbance and $e^{N(s^*,f)}$ is the exponentiated amplification factor (N-factor) determined through LST analysis for a given frequency $f$ and a streamwise location $s^*$. The nondimensional amplitude $A(s^*, f)$ is derived by normalizing the local surface pressure perturbation at a given frequency by the freestream density perturbation of the same frequency in the pulse, as defined in Eq. 19.

$$\frac{|dP(f)/P_\infty|}{|d\rho_\infty(f)/\rho_\infty|} \tag{19}$$

This normalization accounts for the nonuniform frequency distribution of disturbance amplitudes in the freestream pulses. The N-factor and perturbation data are sampled at the same streamwise position. It is observed later that the choice of sampling location does have some influence on the resulting receptivity coefficients due to the influence of freestream forcing.

The decomposition method used in this work is relatively simple and has been shown to be effective for flows that are strongly dominated by second modes[26]. However, very blunt cones generally experience significantly weaker second mode amplification and are much more strongly influenced by multimodal effects. More rigorous modal decomposition methods, such as the bi-orthogonal decomposition used by Tumin[42] and Miselis[43] may be necessary to decompose the receptivity spectra of much more complicated boundary layer disturbance profiles into their modal components. This rigorous modal decomposition would provide additional much needed insight into the physics of hypersonic flows over aerodynamic geometries, though further development of these tools is required.

## V. Steady Flow Field Solution

The steady DNS pressure and temperature meanflow contours for the cone are shown in Fig. 3a for the first and second computational zones near the nose and the beginning of the cone frustum. For clarity, the grid plot in Fig. 3b was coarsened by a factor of 4 in both the $\xi$ and $\eta$ directions. A total of 240 points were used in the $\eta$ direction, while the distribution in $\xi$ ranged from 30 points per mm at the nose to 5 points per mm at the end of the geometry. These distributions were chosen to ensure that sufficiently large wavenumber disturbances could be captured by the simulation and to provide sufficient resolution in the meanflow data so as to reduce numerical inconsistencies in the LST analysis. A total of 10,080 points were used in the $\xi$ direction to resolve the cone to 1.9 m. Marineau[36] studied cones up to lengths of 1.5m. The domain here was lengthened to allow for the development of a more amplified second mode which would be use to generate spectral receptivity data for the studied pulse disturbances.

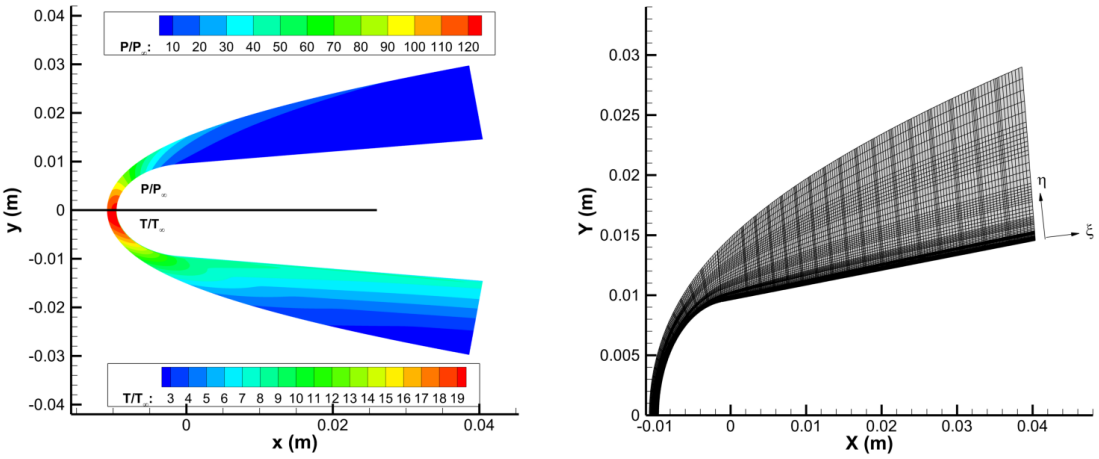


(a) (b)

**Fig. 3 Partial view of (a) pressure (top) and temperature (bot) contours and (b) grids for zones 1 and 2 near nose region.**

Similar pressure and temperature contours for the full cone are shown in Fig. 4. The temperature contours in Fig. 3a and Fig. 4 show an entropy layer extending to approximately $x = 1.0$ m before merging with the boundary layer. These entropy layers reduce local flow velocities, and in turn reduce local Reynolds numbers. Since transition locations have been correlated with larger local Reynolds numbers, this process has been used to explain the transition delaying mechanism for intermediate nose bluntness[44]. However, this fails to explain transition reversal effects observed in large bluntness flows[25]. Zhong and Ma[18] observed the emergence of an additional generalized inflection point in the entropy layer of their blunt cone which may be indicative of inviscid instability. These entropy layer instabilities can be absorbed by the boundary layers in blunt cones and potentially lead to early transition, though they have been observed to be relatively weak in perfect gas flows. They also pointed out that non-modal instabilities may have stronger

influence in blunt cones, and cause this reversal. Similarly, Balakumar and Chou [21] observed large oscillations in the entropy layer before second mode disturbances eventually began to dominate further downstream on their straight blunt cone cases. Further investigation of the effects of freestream receptivity in the entropy layer may be of interest in resolving this problem.

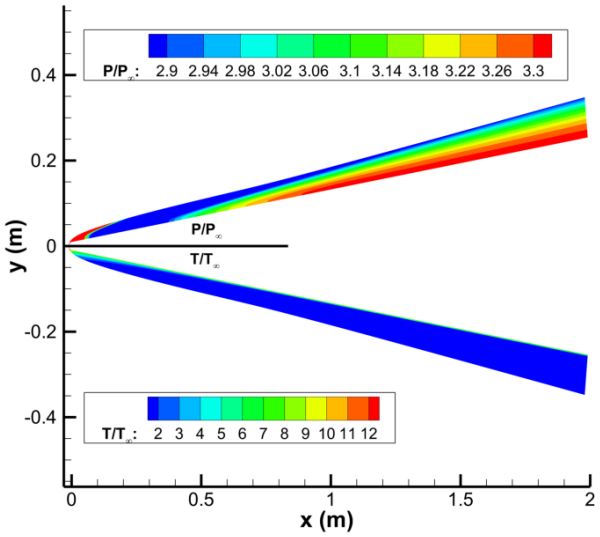


**Fig. 4 Meanflow pressure (top) and temperature (bot) over the entire cone.**

The wall-normal profiles of both velocity and entropy are presented in Fig. 5. The velocity profiles in Fig. 5a demonstrate weak variation in boundary layer height after approximately $s^* = 0.7405$ m, supporting the locally parallel assumption used for LST. The extent of the entropy layer is further defined in Fig. 5b in which it is shown to extend above the boundary layer across much of the cone. The entropy layer and boundary layer are observed to merge near approximately $s^* = 0.9881$ m.

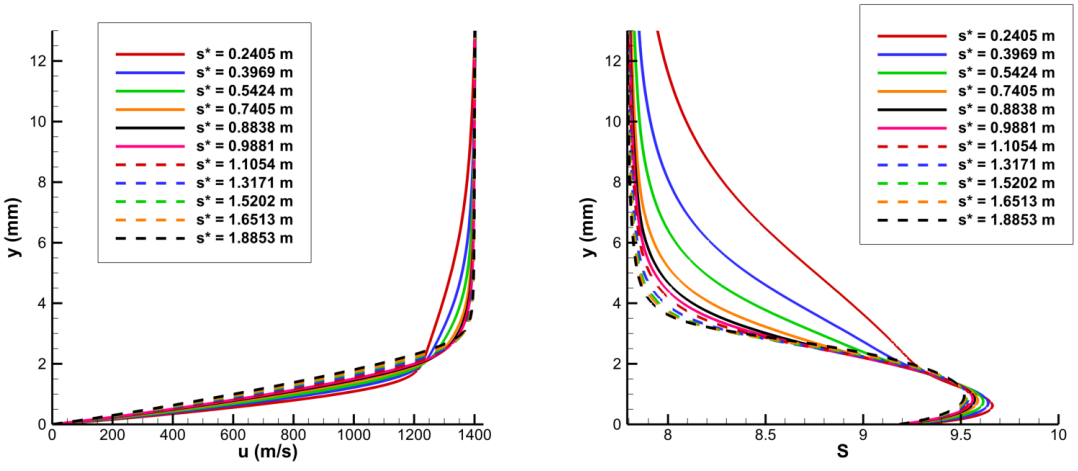


(a) (b)

**Fig. 5 Wall normal (a) U velocity and (b) S entropy profiles at different positions along the cone.**

The convergence of the meanflow simulation is validated by comparing the current 240 point grid in the wall normal direction with a further refined 480 point result. This refinement is only done in the wall normal direction because flow

variable gradients in this direction are particularly extreme for high-speed wall-bounded shear flows. In particular, the boundary layer must be sufficiently well resolved in order to ensure accurate analysis of disturbances. The results of this convergence study are shown in Fig. 6 for wall normal velocity and temperature profiles at a streamwise location of $s^* = 0.705$ m.

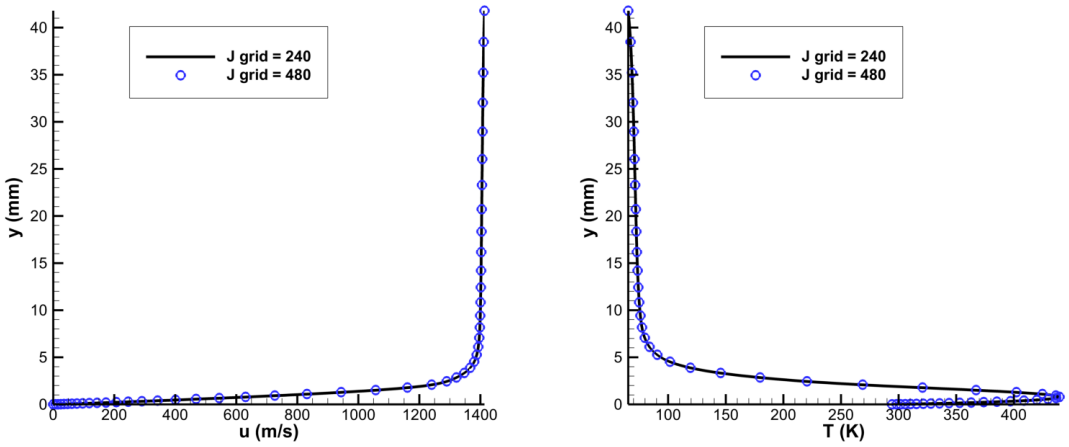


(a) (b)

**Fig. 6 Grid convergence comparison of wall normal (a) U velocity and (b) T temperature profiles at $s^* = 0.705$ m.**

The profiles of the current 240 point grid and the refined 480 point grid qualitatively look nearly identical, implying convergence. The difference between the two grids can be further quantified by the infinity norm of the relative error, which is defined as the maximum error in the temperature or velocity profile. The infinity norm based on the velocity is $1.65 \times 10^{-6}$.

## VI. LST Results

LST results indicate a strong amplified second mode band between frequencies of 118 kHz and 238 kHz. At the reported experimental transition location of 1.037m for this case[36], the unstable second mode is found between frequencies of 150 and 185 kHz and compares well to Marineau's results. The growth rate contours and the neutral stability curve is shown in Fig. 7 where $-\alpha_i > 0$ growth rates inside the curve correspond to the unstable second mode region. The neutral stability curve was generated by fitting the branch I and branch II neutral stability points and is highlighted in black.

By integrating the spatial growth rates of discrete frequency second mode disturbances along the streamwise direction using Eq. 4, the total amplification of these disturbances can be calculated. These amplification ratios are known as the N-factors, which are presented in Fig. 8 for a subset of disturbance frequencies ranging from 120 to 240 kHz. Also shown is a comparison of the total N-factor profile against Marineau et al.'s[36] results.

For this case (corresponding to Run 3752), Marineau et al[36] reported an experimentally determined transition location of $s = 1.037m$, along with a corresponding N factor of 1.6. A direct comparison between the LST N-factors in Fig. 8a and Marineau's PSE derived N-factors are shown in Fig. 8b, which was made by fitting the curve profiles for each of the sampled LST frequencies. The LST results of this study report an N-factor of approximately 1.7 at the experimental transition location and are consistent with Marineau's results for this case. In general, the LST results correlate reasonably well with the PSE data reported by Marineau, with our LST overpredicting the N-factors slightly throughout the downstream sections of the domain. This difference can be attributed to non-parallel effects that the LST formulation neglects compared to the PSE algorithm utilized by Marineau.

The phase speed and growth rate of the 150 kHz disturbance in particular are presented in Fig. 9 and are used later to validate the unsteady DNS results. This disturbance frequency was chosen because it was observed to contain a highly amplified second mode. It is shown that the primary second mode disturbance corresponds to the discrete mode

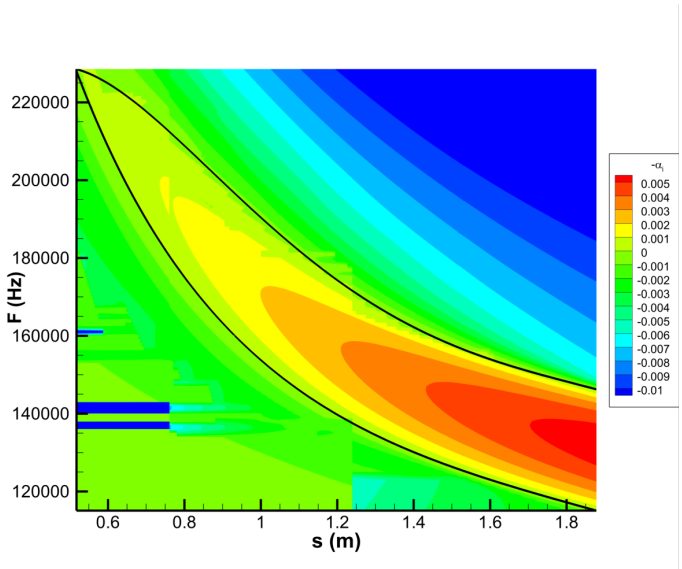


**Fig. 7 LST growth rate contour and neutral stability curve.**

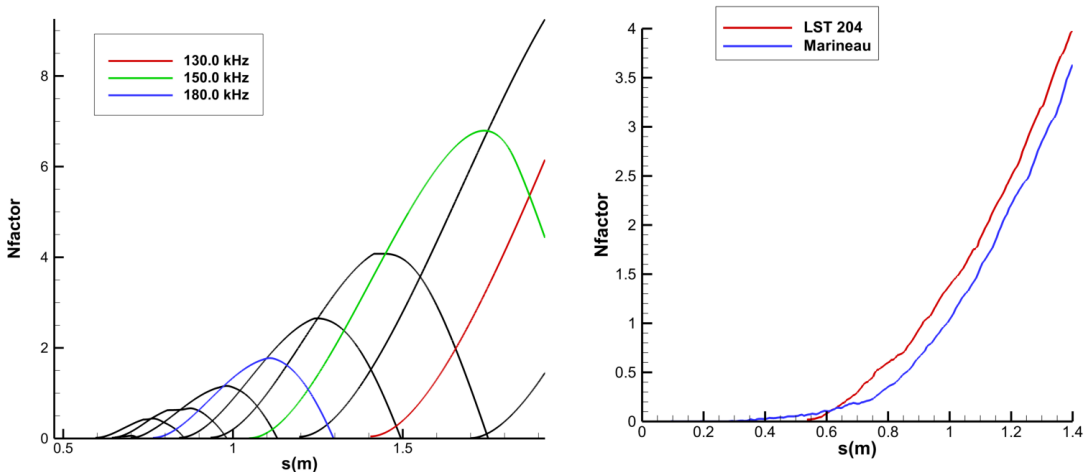


(a) (b)

**Fig. 8 (a) N-factor data ranging between 120 kHz to 220 kHz with $\Delta f$ = 10 kHz. (b) Current LST N-factors vs. Marineau's[36] reported PSE N-factors.**

F emerging from the continuous fast acoustic spectrum. The continuous spectra are indicated in the phase speed plot by the dashed lines at $1 + 1/M_\infty$ for the fast acoustic, 1 for the entropy/vorticity, and $1 - 1/M_\infty$ for the slow acoustic modes. Additionally, Fig. 9 shows that this particular frequency demonstrates an extensive synchronization region between mode F and mode S, lying between 1.1 and 1.7 m along the cone. The discontinuities at $s = 0.8m$ in Fig. 9 can be attributed to issues in the numerical resolution of the LST algorithm near synchronization.

## VII. Unsteady DNS Results

The receptivity of the cone was studied in response to a variety of broadband, continuous frequency freestream disturbances. To do this, the pulse disturbances described in section IV.C were introduced in the freestream. These pulses were then allowed to advect along the central axis of symmetry in the streamwise direction over the meanflow.

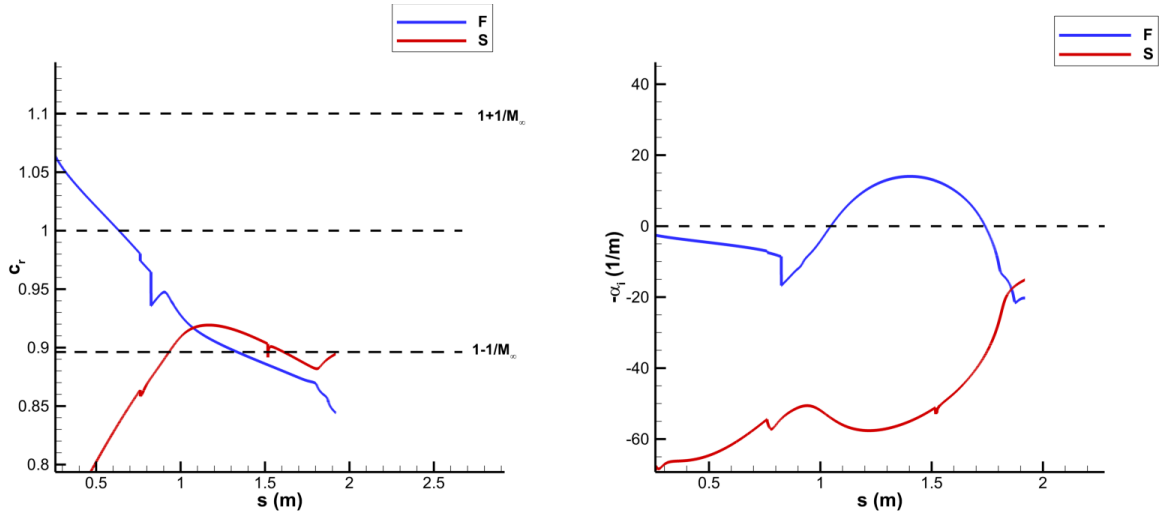


(a) (b)

**Fig. 9 Streamwise LST results at f = 150 kHz for (a) Phase Speed (b) Growth Rate.**

**Table 3 Freestream disturbance cases for unsteady DNS.**

| Disturbance Type | Case |
|---|---|
| *Finite Spherical Fast Acoustic* | B1 |
| *Finite Spherical Slow Acoustic* | B2 |
| *Finite Spherical Temperature* | B3 |
| *Finite Spherical Vorticity* | B4 |
| *Planar Fast Acoustic* | B5 |
| *Planar Slow Acoustic* | B6 |
| *Planar Temperature* | B7 |
| *Planar Vorticity* | B8 |

The resulting boundary layer disturbances on the cone's surface were studied using FFT to decompose the surface pressure perturbations into their spectral frequency components. The specific disturbance cases and their respective labels are given in Table 3. The disturbances are differentiated by both their freestream perturbation type and their geometry. The temperature, fast acoustic, slow acoustic, and vorticity disturbances are defined by the freestream dispersion relations in Eq. 6, 9,10, and 11 respectively. The amplitude spectra of the pulses were fixed to be the same within the finite spherical and planar cases respectively.

### A. Finite Spherical Pulse Unsteady DNS Results

Fig. 10 for the finite spherical fast acoustic pulse (Case B1) shows the pressure disturbance contours at a downstream position on the cone. The rope-like wave structures shown here are indicative of a perturbation growing in accordance with Mack's second mode[4]. These boundary layer disturbances were qualitatively observed in each case considered in this study and indicate strong second mode amplification downstream on the cone.

In addition to the conventional second mode, mach wave-like radiating structures can be observed near the tail end of the disturbance wavepacket. This behavior is characteristic of a supersonic mode, in which the phase speed of the disturbance is supersonic with respect to the mean flow[45]. Recent studies have shown that these supersonic modes may have disturbance amplitudes similar in strength to second mode instabilities, and as a result may be of significant

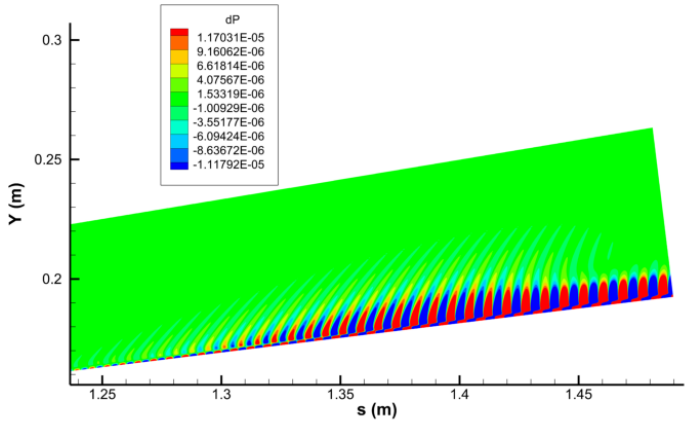


**Fig. 10 Pressure perturbations near s = 1.5 m after the finite spherical fast acoustic perturbation (Case B1).**



importance in the process of transition [45–48]. However, similar to Reshotko[2] and Mack[49] the supersonic mode seen here is relatively weak and emerges far enough downstream on the cone that it isn't likely to effect transition. This supersonic mode may still play a role in downstream phenomena such as nonlinear breakdown, and is of continued interest.

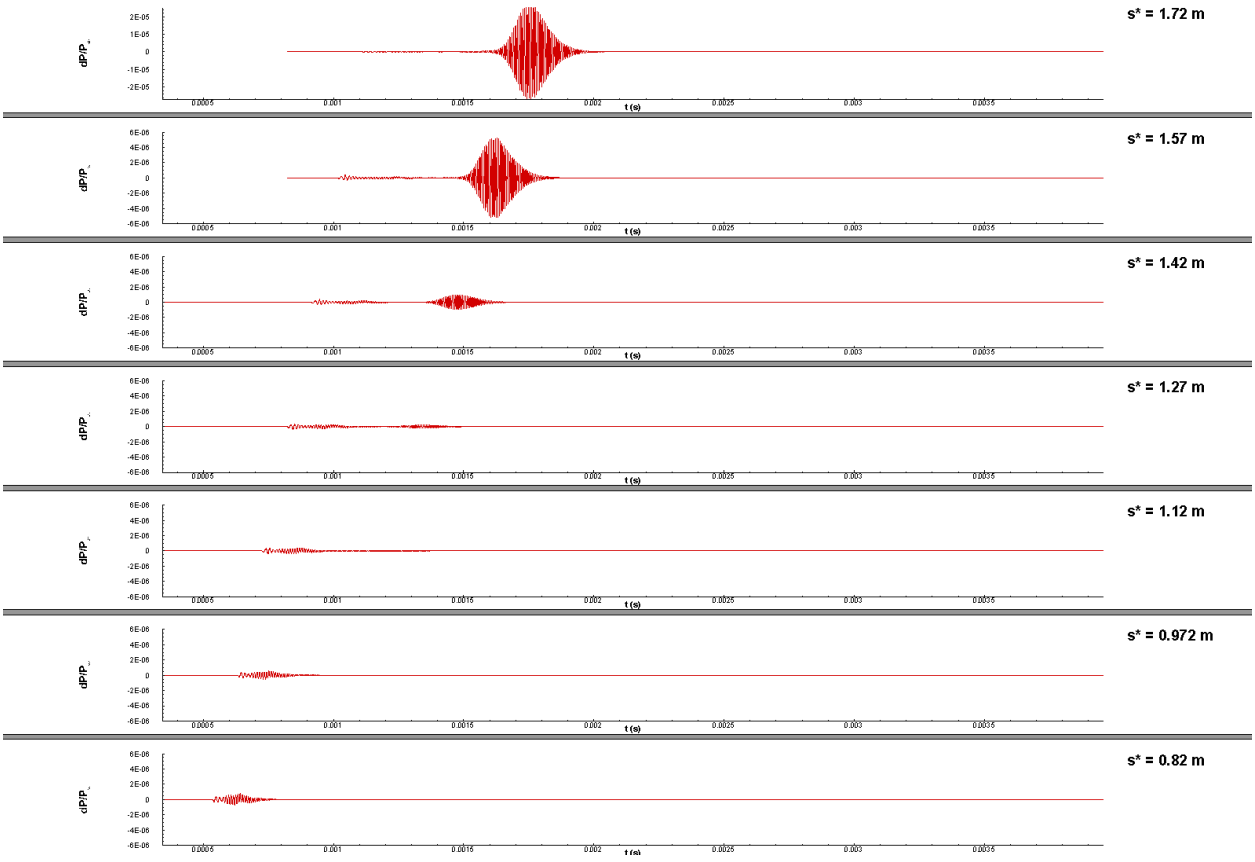


**Fig. 11 Time history of normalized surface pressure perturbations resulting from finite spherical fast acoustic pulse disturbance (Case B1).**

The normalized surface pressure perturbations along the cone after excitation by a finite spherical fast acoustic

pulse (Case B1) are presented in Fig. 11 for a selection of streamwise positions. Before the second mode region, the wavepacket is incoherent and is dominated by oscillations associated with non-modal forcing. These forcing waves are shown to decay upstream of the second mode region before experiencing significant amplification of the second mode as they propagate downstream. The increasingly coherent wavepackets seen after $s^* = 1.42$ m are indicative of the presence of a dominant second mode instability.

The total surface disturbances depicted in Fig. 10 and Fig. 11 may be studied more quantitatively through the use of Fourier decomposition. The surface perturbation signal is decomposed into its discrete frequency disturbances using a Fast Fourier Transform (FFT). The resulting normalized surface pressure contour maps for the finite spherical fast acoustic (Case B1), slow acoustic (Case B2), temperature (Case B3), and vorticity (Case B4) disturbances are shown in Fig. 12. These Fourier decomposed pressure disturbances are normalized by the spectral content of the initial freestream disturbance shown in Fig. 2b to account for the non-uniform frequency distribution of the initial pulse[26]. Additionally, the LST neutral curve is also plotted in solid black lines in these figures in order to validate the unsteady results. The most amplified frequency was observed to be approximately 155 kHz and agrees well with the LST N-factor results presented previously. The neutral curves align as expected with the band, since peak unsteady amplification for the second mode disturbance should be centered about the branch II neutral line[45]. Thus, while LST does not account for the effects of freestream forcing, the resultant downstream perturbation spectra are shown to be dominated by the modal instability predicted by LST and the neutral curve is observed to be relevant to the amplification behavior of the primary instability of the flow.

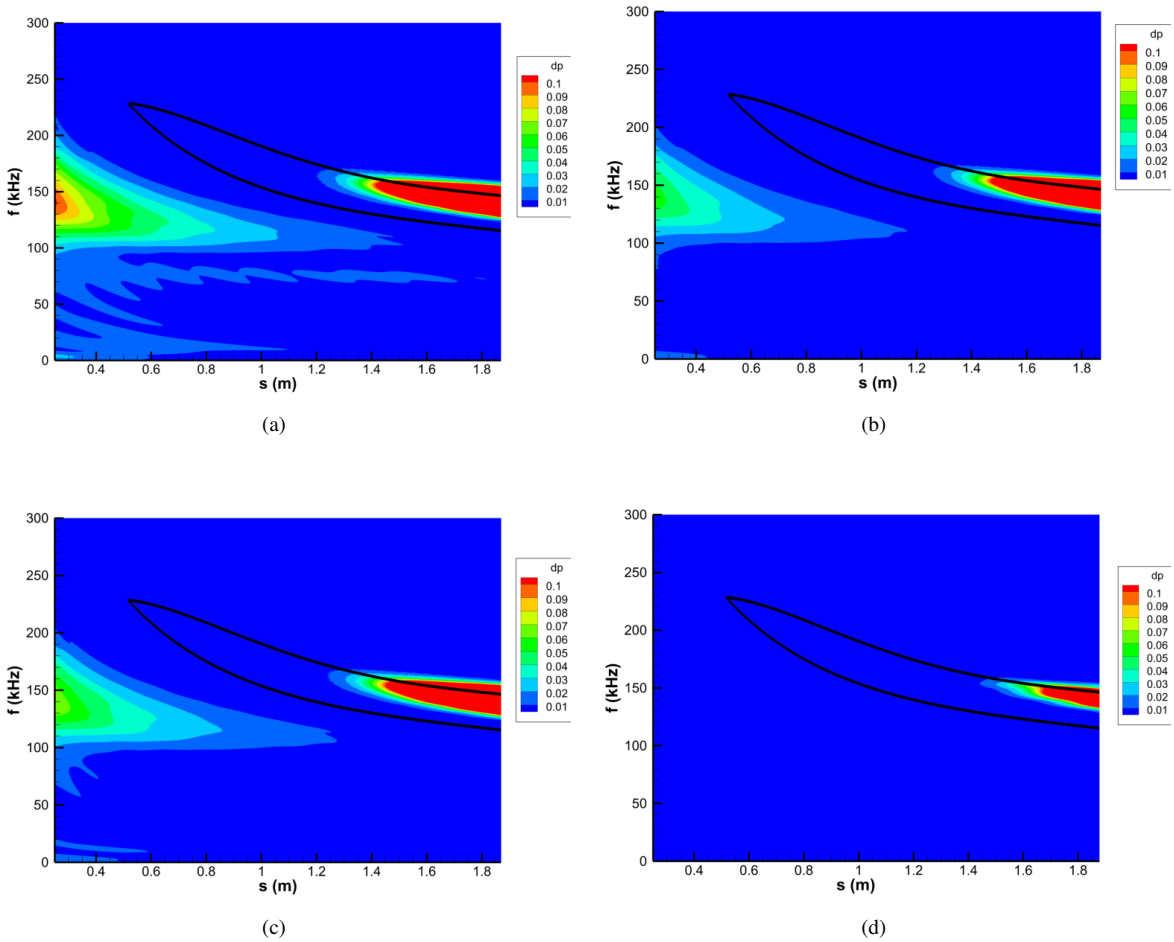


**Fig. 12 Surface FFT pressure distribution for (a) Case B1, (b) Case B2, (c) Case B3 and (d) Case B4.**

Fig. 12 shows that the four finite spherical pulses similarly excite the second mode in the downstream portions of the

cone. The primary band of instabilities observed in all four cases is centered between approximately 140 and 170 kHz, depending on streamwise position. An additional disturbance band between 100 kHz and 200 kHz is observed at the beginning of the domain in cases B1 through B3 and corresponds to the forcing waves generated by the shock-disturbance interaction upstream. A similar phenomenon is observed in Case B4 as well, though the general receptivity of the meanflow to freestream vorticity disturbances is weak enough that this forcing cannot be seen in the uniform contour levels in Fig. 12d. Similarly to Fig. 11 these initial lower frequency perturbations are attenuated until the second mode region, where modal amplification begins. Both the initial forcing and the second mode disturbance amplitudes were strongest for the finite spherical fast acoustic disturbance (Case B1), followed by the temperature (Case B3), the slow acoustic (Case B2), and finally the vorticity (Case B4) disturbances respectively.

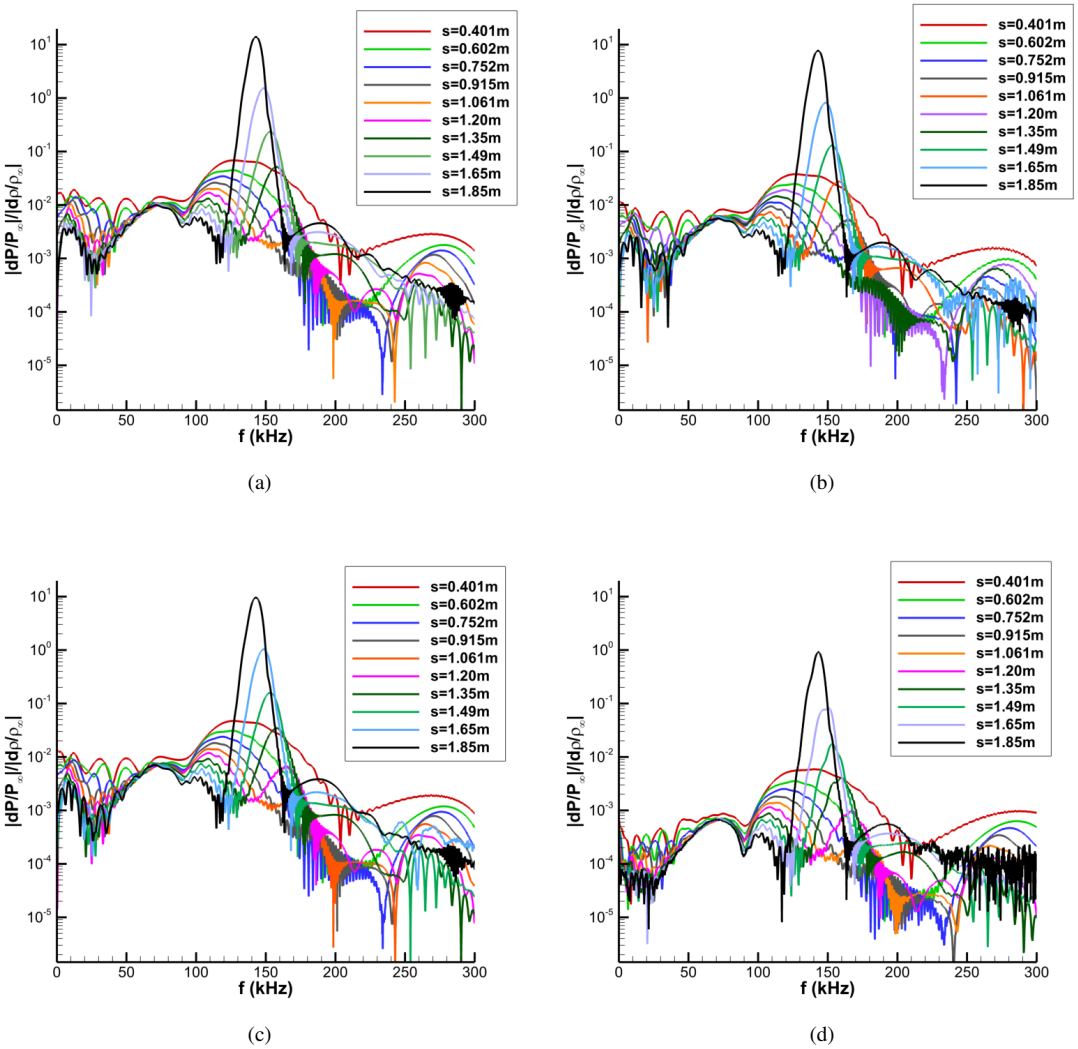


**Fig. 13 FFT decomposed surface pressure spectra at various streamwise locations for (a) Case B1, (b) Case B2, (c) Case B3, and (d) Case B4.**

The FFT decomposed surface pressure perturbations at different streamwise locations both upstream and downstream of the second mode amplification region are also presented in Fig. 13 for Cases B1 through B4. As expected, the spectral surface pressure distributions for the finite spherical cases are very similar to each other. Again, we see that Case B1 excites the strongest overall pressure perturbations downstream in the second mode region. Case B1 is seen again here to generates stronger initial disturbance waves upstream of the second mode amplification region. Distinctive peaks in the disturbance amplitude can also be seen here, initially centered around frequencies of approximately 170-180 kHz.

As the sampling point moves further downstream this peak disturbance band shifts to center around lower frequencies while also growing in overall amplitude, eventually centering around 145-155 kHz near the end of the computational domain. The amplitude peaks observed here correspond to the primary second mode instability for this flow. This shift to lower frequencies in the downstream regions can also be seen in the LST results in Fig. 7, as optimal disturbances are expected to follow with the branch II neutral point. The broadband disturbance dampening and amplification pattern is clearly seen again here. While the spectral amplitudes for Cases B2, B3, and B4 are smaller, the same general trends are observed.

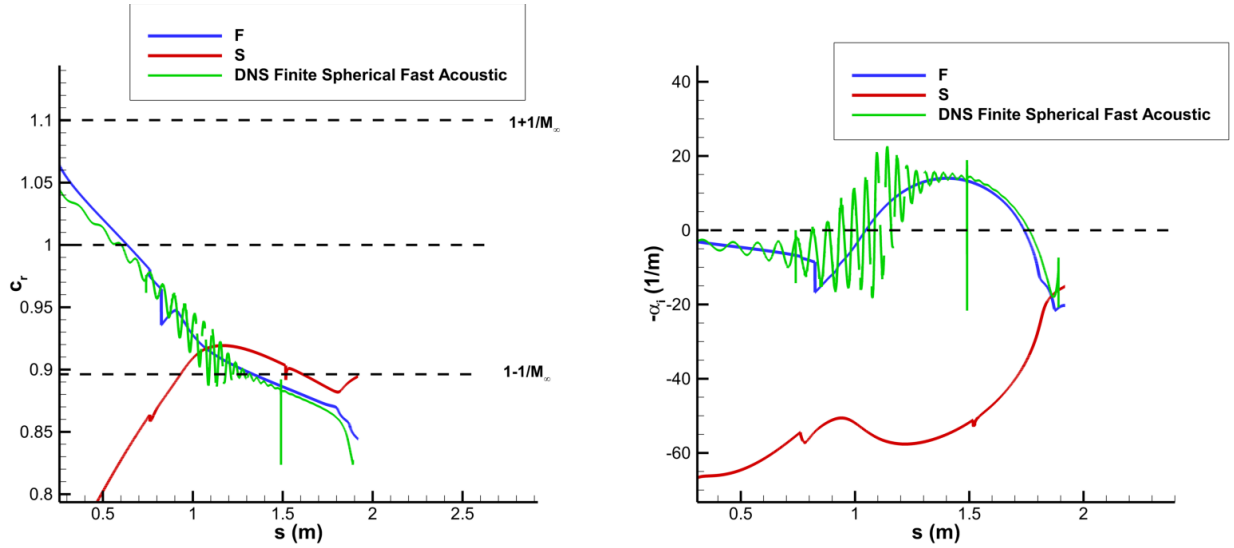


(a) (b)

**Fig. 14 Case B1 unsteady DNS vs. LST predicted results for 150 kHz disturbances (a) Phase Speed (b) Growth Rate.**

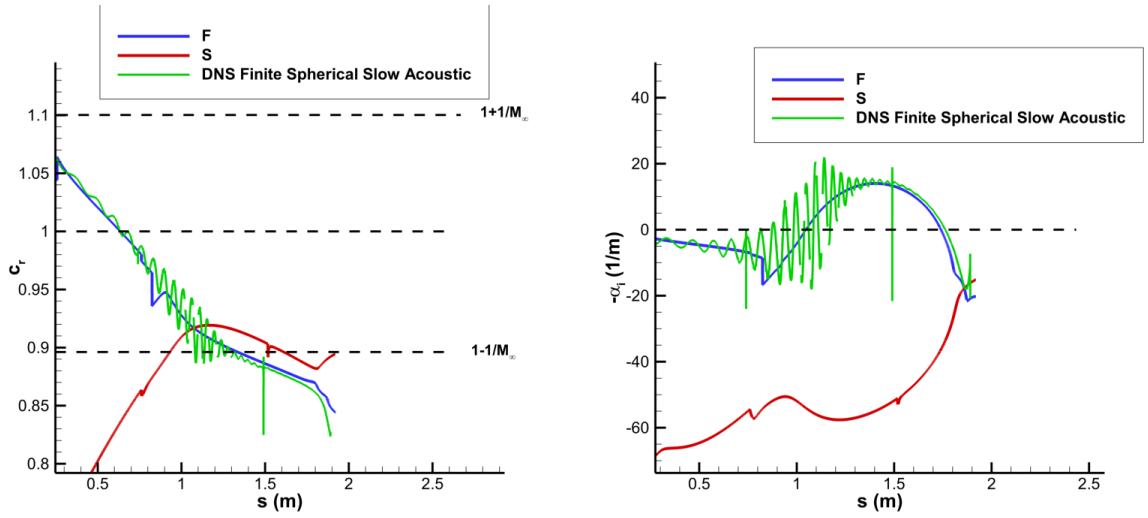


(a) (b)

**Fig. 15 Case B2 unsteady DNS vs. LST predicted results for 150 kHz disturbances (a) Phase Speed (b) Growth Rate.**

Through Eq. 15, 16, and 17 the Fourier decomposed unsteady DNS can be used to calculate the growth rates and phase speeds of different discrete frequency surface perturbations. The 150 kHz frequency disturbance in particular was used in order to validate the results of the unsteady DNS. The results for the 150 kHz frequency disturbance for the finite spherical fast acoustic (Case B1), slow acoustic (Case B2), temperature (Case B3), and vorticity (Case B4) pulses are presented in Fig. 14, 15, 16, and 17 respectively.

The unsteady DNS results for case B1 show good agreement with LST, demonstrating that the discrete mode F is unstable for this case. The LST predicts an extensive synchronization range for this frequency between streamwise locations of 1.1 m and 1.8 m. Near the beginning of the synchronization region, significant oscillations in both the phase speed and growth rates can be observed in the DNS results. This oscillation is indicative of modal interactions associated with the synchronization of the discrete modes, though it is still apparent that the unstable mode F dominates the flow. These oscillations dampen out significantly as the disturbance propagates through the end of the domain for Case B1 in Fig. 14.

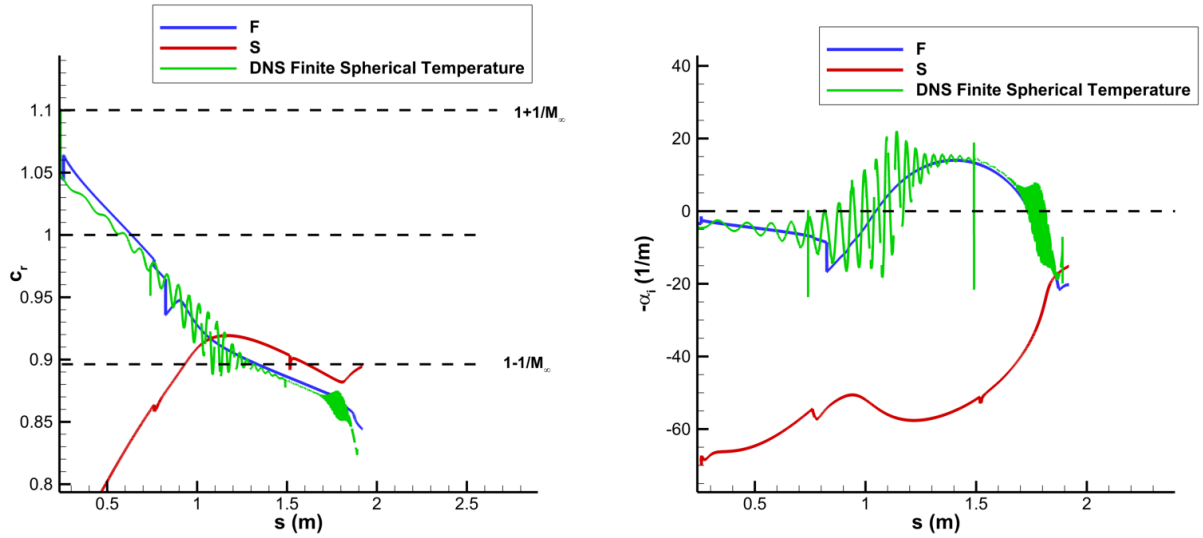


(a) (b)

**Fig. 16 Case B3 DNS vs. LST predicted results for 150 kHz disturbances (a) Phase Speed (b) Growth Rate.**

The results for Case B2 in Fig. 15, Case B3 in Fig. 16, and Case B4 in Fig. 17 similarly follow the unstable mode F disturbance, though strong confined oscillations in the unsteady DNS results are also observed at the end of the synchronization between the discrete mode F and mode S at this frequency for Case B3. This can be attributed to sampling errors, and will be reconverged in the future to eliminate the spurious oscillations.

The unsteady DNS results for the 150 kHz for the finite spherical pulse cases share many similarities. In particular, Case B1 and Case B2 are observed to be nearly identical in their general response. Case B3 on the other hand exhibits significant multimodal oscillations near the end of the domain while Case B4 experiences significantly stronger modulations at synchronization. It can be concluded that while all of the finite pulse cases were observed to significantly excite the second mode, they do not share the same general receptivity response in terms of the total boundary layer disturbance content. While singular discrete frequency disturbance results may be similar between the cases, general broadband disturbance spectra can differ significantly between the different freestream pulses. This necessitates the further study of these generalized disturbances in order to fully characterize the possible responses the meanflow can have to different environmental noise.

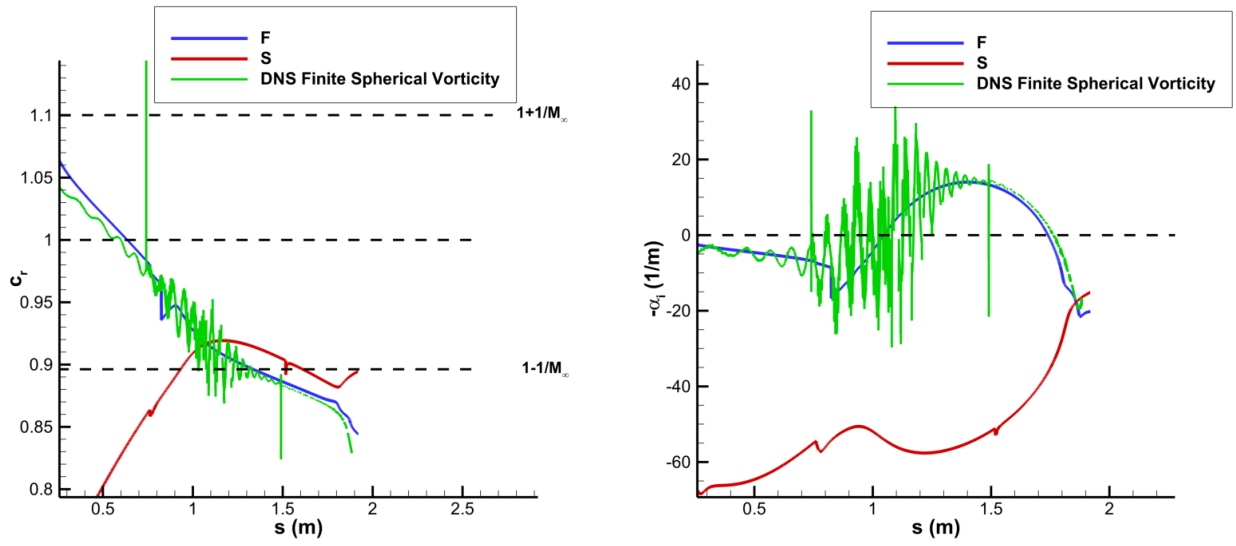


**Fig. 17 Case B4 DNS vs. LST predicted results for 150 kHz disturbances (a) Phase Speed (b) Growth Rate.**

### B. Planar Pulse Unsteady DNS Results

Fig. 18 presents snapshots of the disturbance pressure contours resulting from the planar fast acoustic pulse (Case B5) over a downstream region of the cone at two different times. In particular, Fig. 18a depicts the front of the downstream shock-disturbance interaction and the wake of disturbances it excites while Fig. 18b shows the slower band of amplifying second mode disturbances behind the pulse front. In Fig. 18a a sharp interface can be seen at the leading edge of the disturbance front. This distinctive edge shows significant forcing being generated by the local shock-disturbance interaction which directly propagates to the boundary layer. The result of this forcing can be directly observed in the normalized surface pressure time history plots in Fig. 19. The time history shows a strong secondary disturbance spike caused by the local forcing that propagates throughout each of the downstream regions. Before the second mode region, this local forcing is observed to be highly dominant in the flow field. Even at a relatively downstream position of $s^* = 1.42$ m, the magnitude of the forcing disturbance overshadows that of the amplifying second mode disturbance wavepacket. It is only near the end of the cone where the primary second mode disturbance begins to dominate. Furthermore, this forcing is also observed to experience amplification as it continues downstream, albeit much more weakly than the primary second mode. This amplification can also be explained by the consistent introduction of additional forcing throughout the domain by the planar pulse and the weak/neutral stability of the forcing modes.

The second mode wavepacket depicted in Fig. 18b somewhat follows the trends observed in the finite spherical disturbance cases. Clear rope-like structures denote the existence of the second mode disturbance. The supersonic mode is again observed here for Case B5, though it is shown to extend much farther into the shock layer, indicating a different receptivity response for the supersonic mode in comparison to the finite spherical fast acoustic case (Case B1). The receptivity of supersonic mode disturbances in particular may also be of interest in future work.

Similar results are presented for the planar slow acoustic pulse (Case B6) in Fig. 20 and Fig. 21 which also closely reflect the characteristics of the planar temperature (Case B7) and vorticity pulses(Case B8). The surface pressure disturbance contours in Fig. 20 demonstrate significant differences between Cases B5 and B6. The local disturbance front in Fig. 20a has a much smaller magnitude than Case B5. Furthermore, strong forcing is not observed to propagate directly into the boundary layer in this case. This is reflected in the surface pressure disturbance time history in Figure 21 where a result similar to the finite spherical pulses is observed. The pressure disturbance structures in Fig. 20b also reflect a strong second mode disturbance. However, the acoustic radiation characteristic of a supersonic mode is not observed. While the second mode instability is observed to be universally excited for all of the disturbance cases, the supersonic mode does not. Further studying the receptivity of the supersonic mode in particular may also be of interest in further characterizing the stability behavior of a flow.

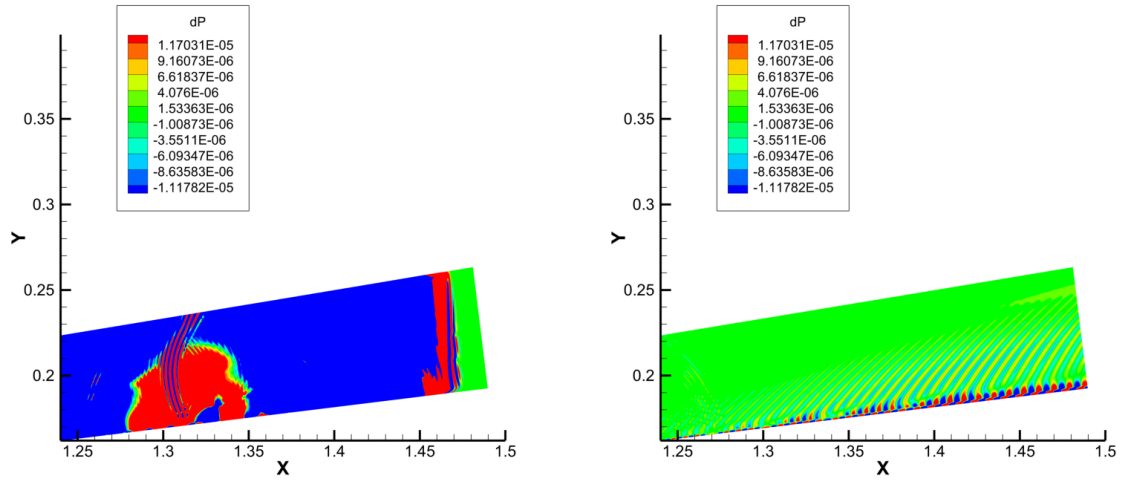


**Fig. 18 Pressure perturbations near s = 1.5 m after the planar fast acoustic perturbation (Case B5) for (a) the pulse front and (b) the primary second mode behind the pulse front.**

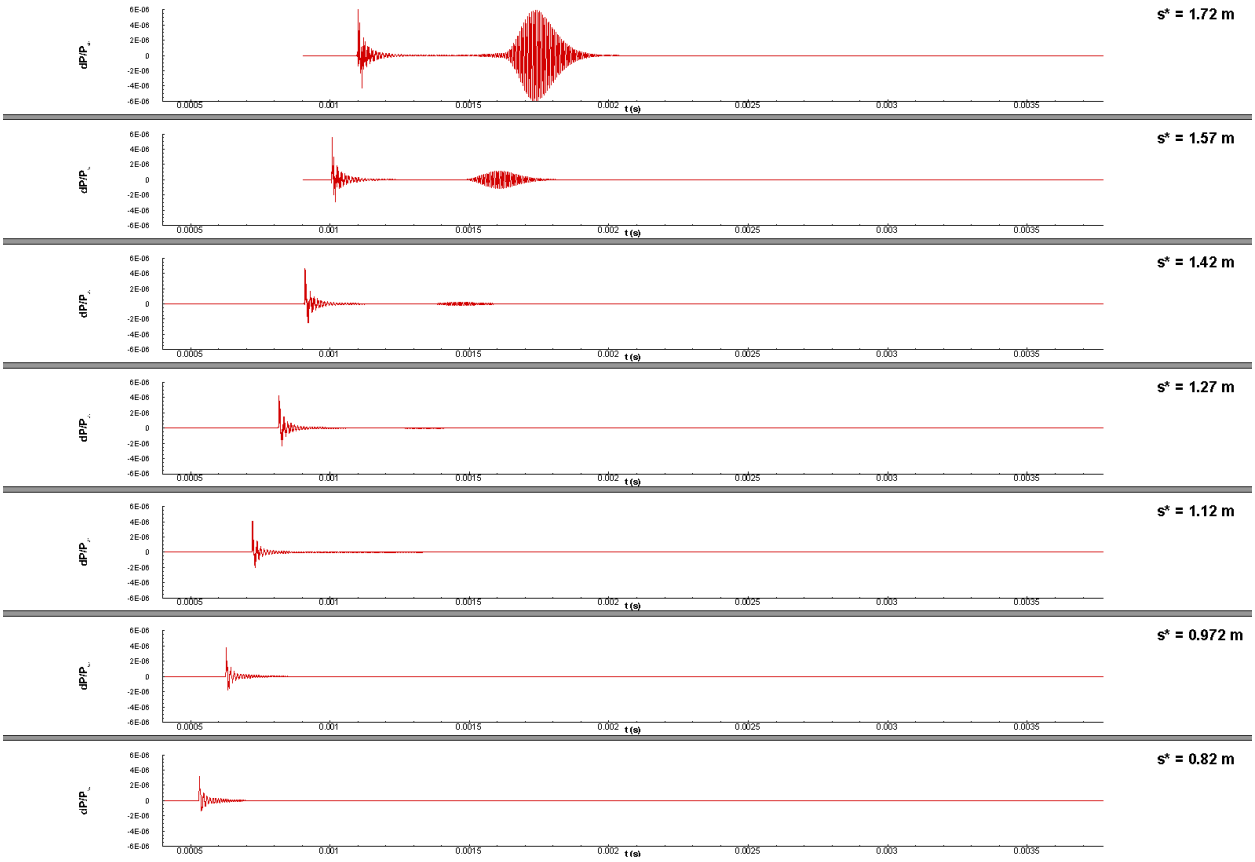


**Fig. 19 Time history of normalized surface pressure perturbations resulting from planar fast acoustic pulse disturbance (Case B5).**

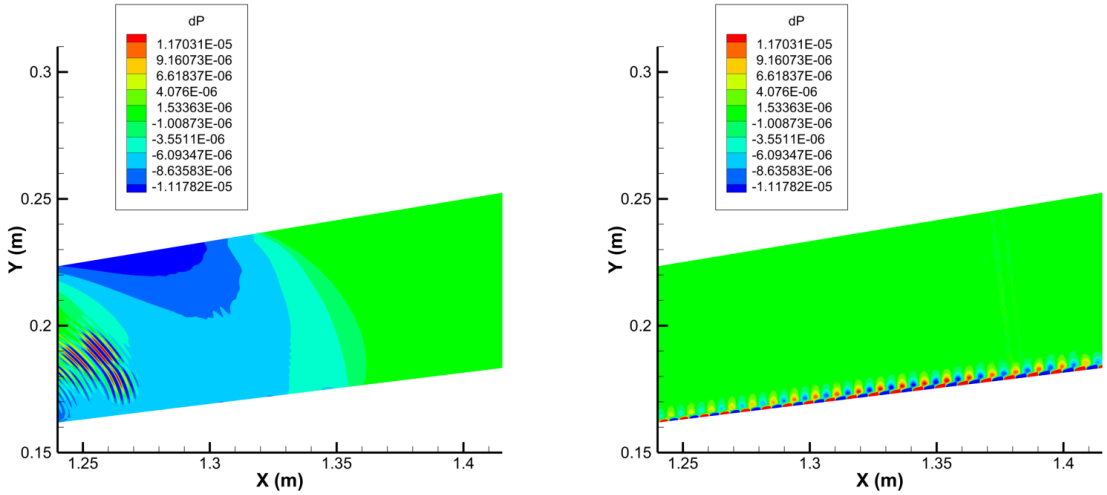


(a) (b)

**Fig. 20 Pressure perturbations near s = 1.5 m after the planar slow acoustic perturbation (Case B6) for (a) the pulse front and (b) the primary second mode behind the pulse front.**

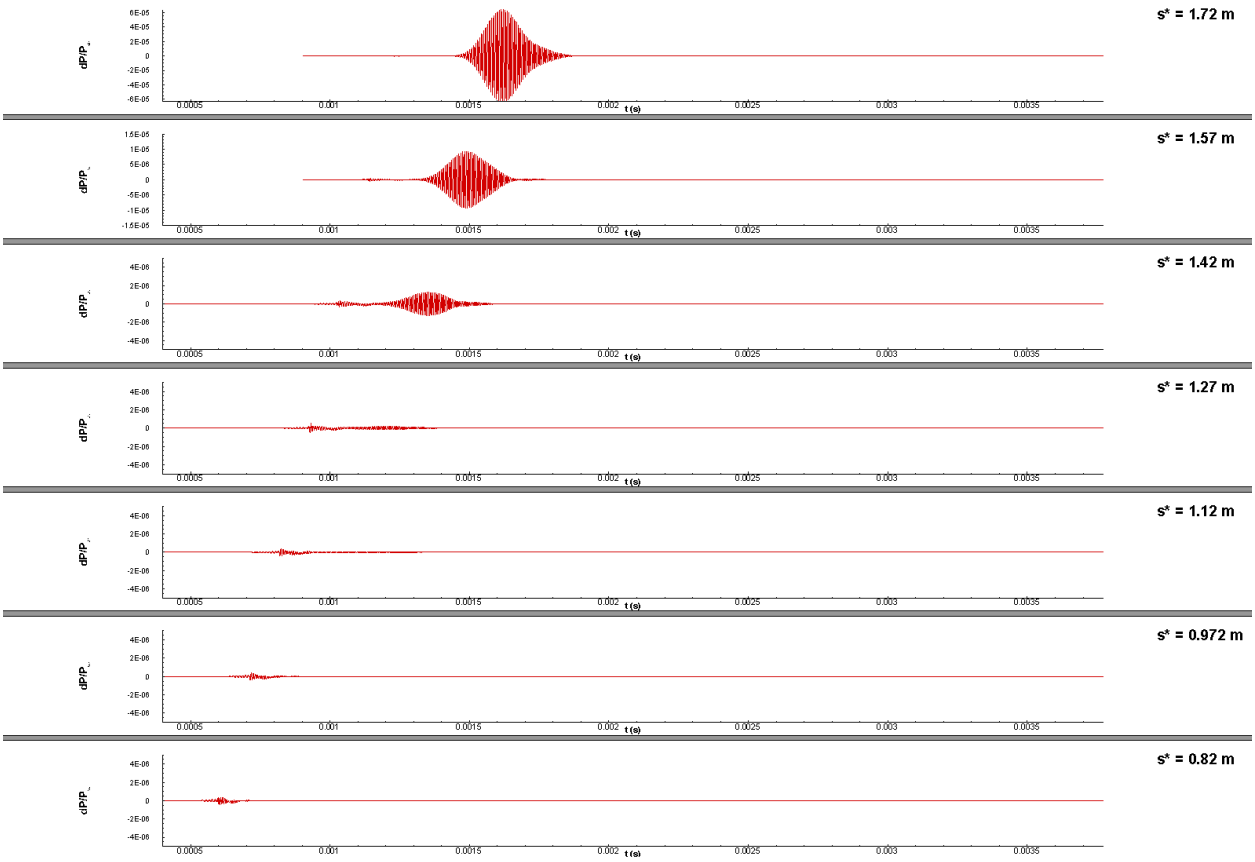


**Fig. 21 Time history of normalized surface pressure perturbations resulting from planar slow acoustic pulse disturbance (Case B6).**

The surface pressure contour maps for the planar fast acoustic (Case B5), slow acoustic (Case B6), temperature (Case B7) and vorticity (case B8) disturbances are presented in Fig. 22. The total surface disturbance spectra share many similarities to the finite spherical pulse cases. In particular, Fig. 22b for Case B6 and Fig. 22c for Case B7 also depict strong initial forcing near the beginning of the plotted domain that is partially attenuated before second mode amplification. Contrary to the finite spherical disturbances, these lower frequency disturbances seem to remain much more significant in the downstream regions of the cone. This is again attributed to the additional forcing provided by the planar pulse. While noise effects are noticeably stronger for the planar cases, they are still observed to strongly excite primary second mode disturbances downstream on the cone. This again implies that the LST amplification predicted amplification behavior still holds.

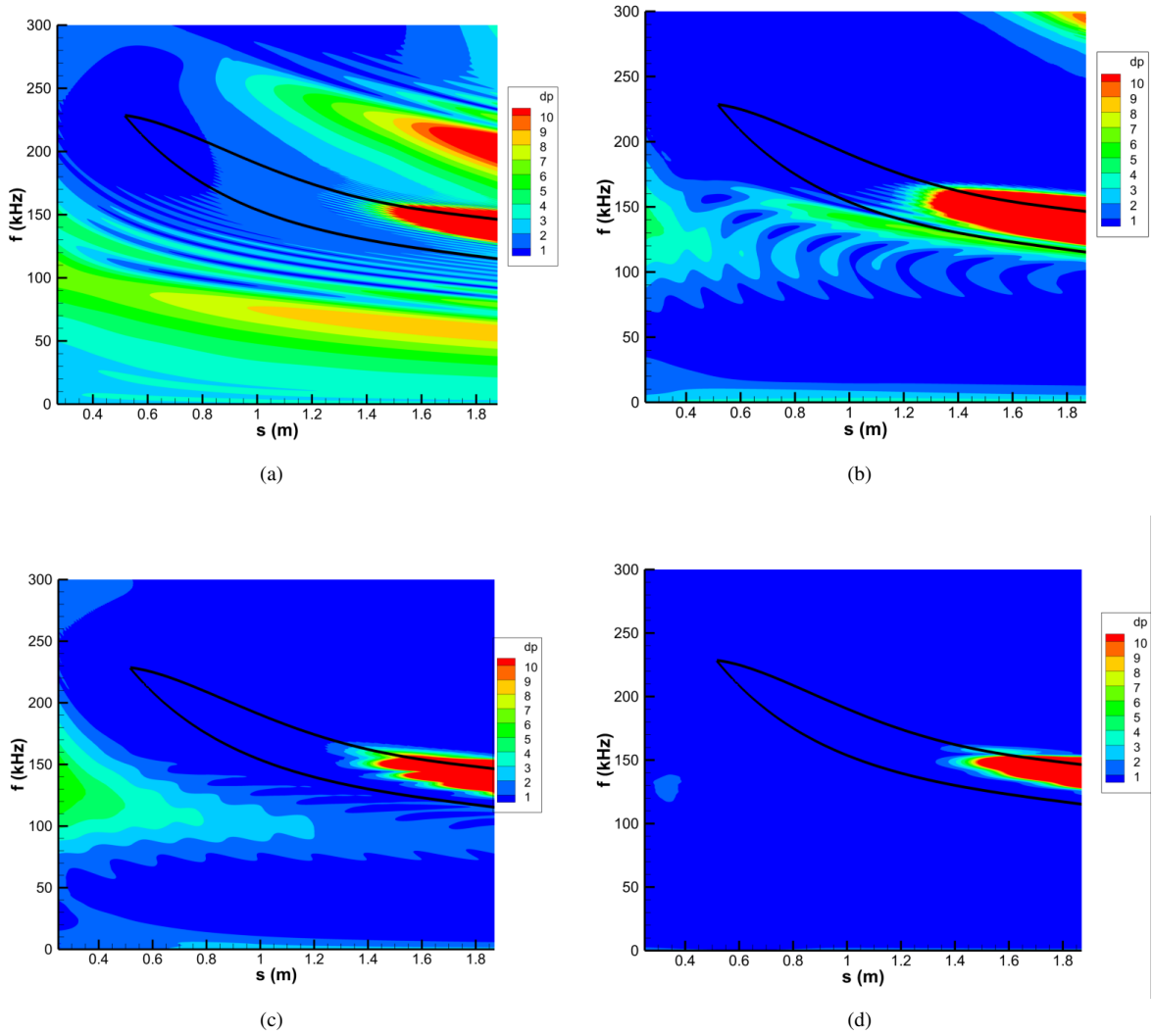


**Fig. 22 Surface FFT pressure distribution for (a) Case B5, (b) Case B6, (c) Case B7, and (d) Case B8.**

On the other hand, the disturbance spectrum for Case B5 in Fig. 22a is significantly more complex. A strong low frequency disturbance band is still observed near 100 kHz while another additional band of unstable frequencies between 180-260 kHz is also apparent. Contrary to the other cases, these additional disturbance bands seem to experience amplification as they propagate downstream through the domain; though the second mode is observed to have the highest amplitudes throughout. These additional disturbance bands may be continuous modes which are excited by the continuous forcing input, and can be observed in the secondary wavepackets in Fig. 19. While these other instabilities

are generally much weaker than the second mode for hypersonic flows[16] at the end of the cone, they may still have considerable impact on the flow. The presence of strong forcing and multimodal disturbances in the planar pulse cases necessitates the use of modal decomposition techniques in order to extract useful receptivity data for instabilities of particular interest, especially in noisy enivronments such as those considered in this study.

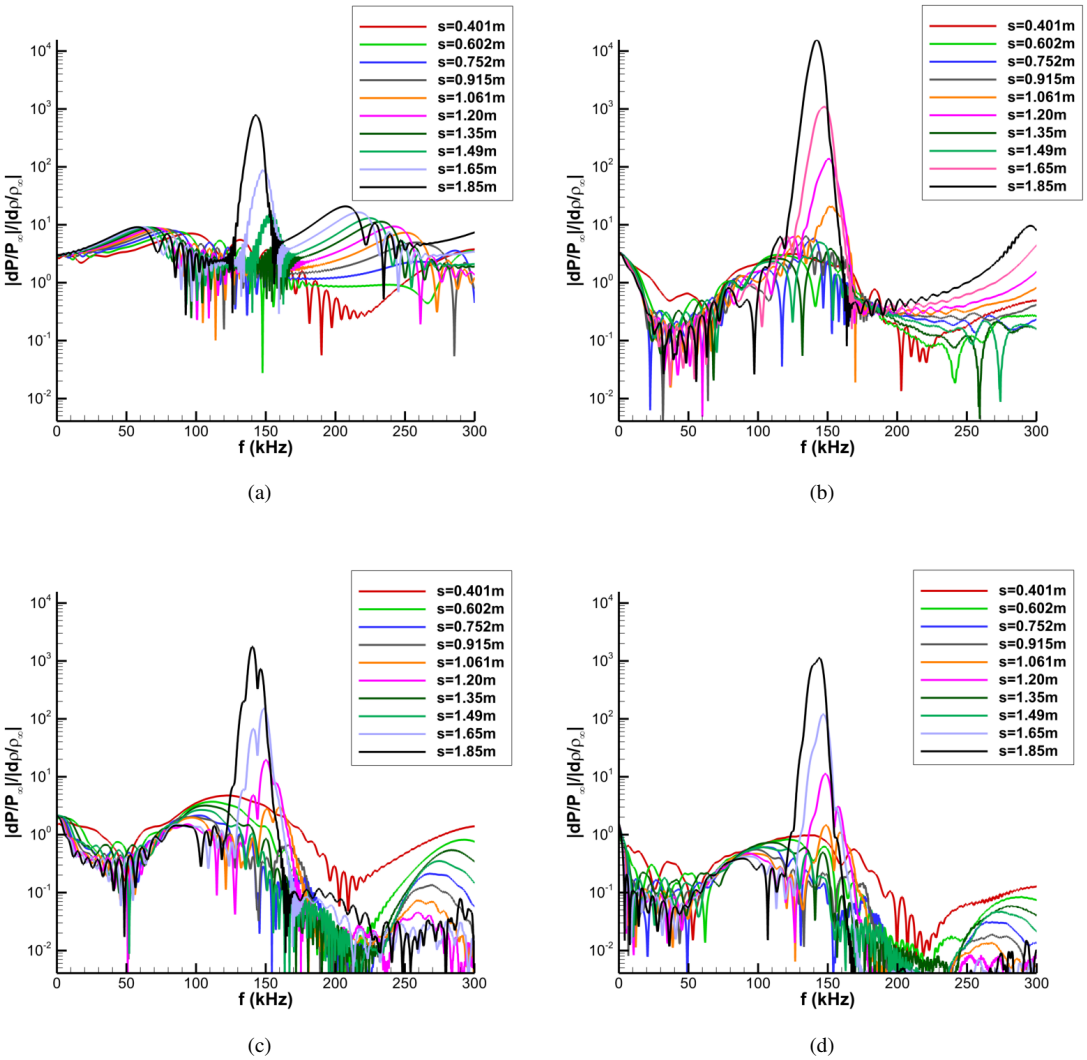


**Fig. 23 FFT decomposed surface pressure spectra at various streamwise locations for (a) Case B5, (b) Case B6, (c) Case B7, and (d) Case B8.**

The normalized surface pressure spectra at different streamwise locations for Cases B5-B8 are shown in Fig. 23. Case B5 in Fig. 23a follows closely with the behavior observed in the finite spherical cases. However, the magnitudes of the second mode peaks are significantly smaller than those for Case B6 in Fig. 23b. The peak second mode amplitude for Case B5 is, however, of similar magnitude to those observed for Case B7 in Fig. 23c and for Case B8 in Fig. 23d. Cases B6-B8 share very similar forcing structures outside of the second mode frequency band between 0 and 50 kHz and between 250 to 300 kHz. Case B5 is also observed to have significantly higher disturbance amplitudes outside of the second mode frequency range. In particular, the low frequency forcing near 50 kHz is between two to three orders of magnitude higher for Case B5 than any of the other planar pulse cases. Furthermore, the disturbance frequencies between 200-250 kHz are also shown to experience amplification as the pulse propagates downstream for Case B5 and are up to three orders of magnitude stronger than similar frequencies in the other cases. This indicates that the receptivity response for Case B5 seems to distribute the forcing in a broadband manner rather than directly excite the

second mode in particular. Case B6 seems to excite traditional discrete mode instabilities in the boundary layer much more strongly than the other disturbance cases, though again Case B7 and B8 produce very similar spectral surface perturbation profiles.

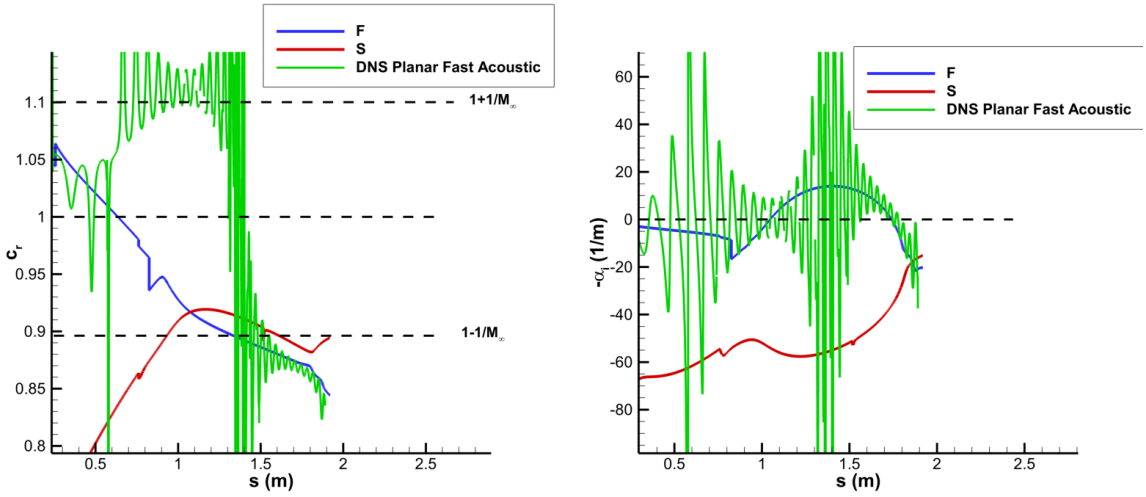


**Fig. 24 Case B5 unsteady DNS results vs. LST predicted results for 150 kHz disturbances (a) Phase Speed (b) Growth Rate.**

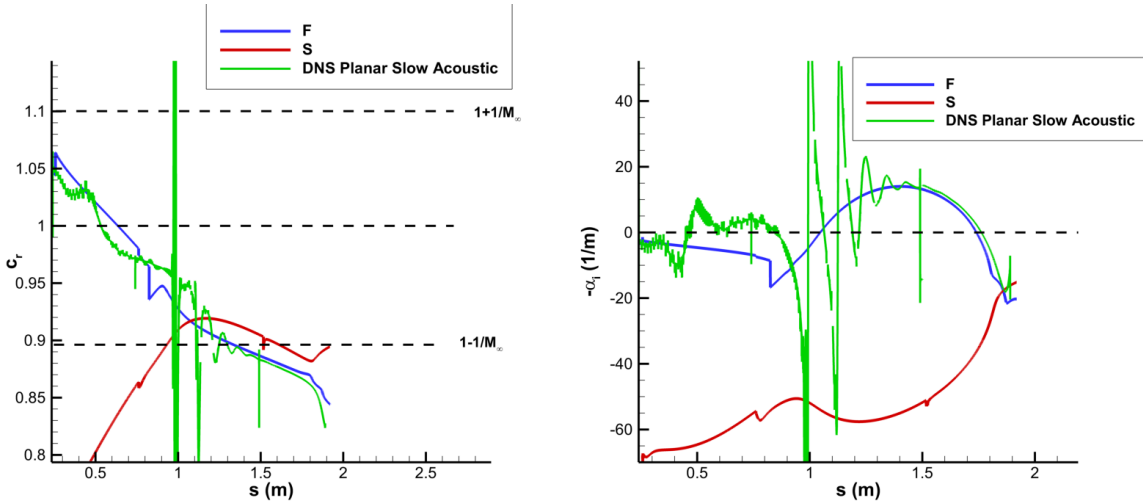


**Fig. 25 Case B6 unsteady DNS results vs. LST predicted results for 150 kHz disturbances: (a) Phase Speed (b) Growth Rate.**

The DNS and LST phase speed and growth rate comparisons for the 150 kHz disturbance are also given in Fig. 24 for Case B5, Fig. 25 for Case B6, Fig. 26 for Case B7, and Fig. 27 for Case B8. The boundary layer disturbances resulting from Case B5 do not seem to become dominated by second mode instabilities until the far downstream regions of the cone. The growth rate shown in Fig. 24b is highly oscillatory and centered around a neutrally stable disturbance until approximately $s^* = 1.6m$. Furthermore, the phase speed plot in Fig. 24a shows similar oscillations centered around the continuous freestream fast acoustic spectrum until the same point and further indicates the dominance of freestream

forcing for Case B5.

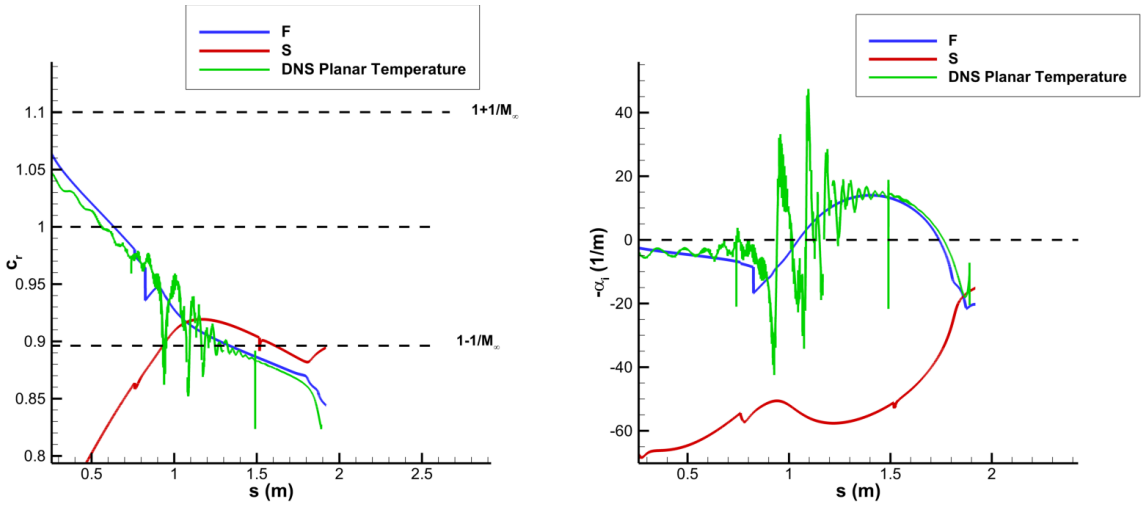


(a) (b)

**Fig. 26 Case B7 unsteady DNS results vs. LST predicted results for 150 kHz disturbances: (a) Phase Speed (b) Growth Rate.**

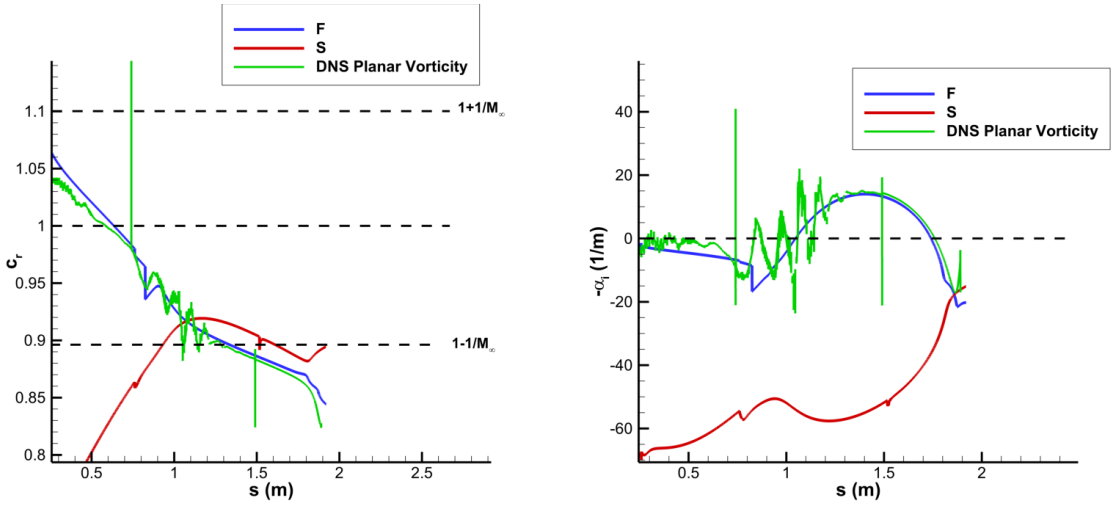


(a) (b)

**Fig. 27 Case B8 unsteady DNS results vs. LST predicted results for 150 kHz disturbances: (a) Phase Speed (b) Growth Rate.**

Case B6 is shown to correlate much better with the 150 kHz LST results with Fig. 25a demonstrating strong agreement with the LST phase speed. The growth rate shown in 25b further corroborates this, though the results prior to 1.4 m still show signifcant oscillations. These oscillations are primarily centered about the synchronization point again, and are generated from the multimodal energy exchange that initially causes the second mode to become unstable. From this it can be seen that Case B6 behaves similarly to the finite spherical disturbances and primarily excites the second mode instability at this frequency, though multimodal effects are much stronger due to the more extensive noise environment. Case B7 in Fig. 26 and Case B8 in Fig. 27 responded similarly for the 150 kHz disturbance. In fact, the modulation was significantly weaker in amplitude for these cases compared to Case B6, indicating weaker multimodal

exchanges in the receptivity response for these pulses.

## VIII. Receptivity Results

The spectral receptivity coefficient for each of the disturbances was calculated from Eq. 18 using surface pressure perturbation data normalized by the freestream pulse amplitude spectra. Using a method was originally proposed by Huang and Zhong[9, 26], the receptivity coefficient is extracted using LST-derived N-factors to extract the initial second mode amplitudes from the unsteady DNS data. Isolating the contributions of different modal disturbances to the total initial disturbance allows for greater specificity when tracking the development of instabilities across a flow domain, especially in cases with significant multimodal content. More rigorous methods for decoupling the modal boundary layer disturbances like the biorthogonal decomposition method developed by Tumin[42] and utilized by Miselis et al.[43] may be necessary to decompose more complex boundary layer disturbance profiles. However, this more rigorous decomposition model requires additional development before it can be applied to the results here.

### A. Receptivity Coefficient Spectra

Using Huang and Zhong's[26] method, the receptivity coefficients were calculated for each of the disturbance cases. Since these receptivity calculations may be sensitive to sampling location, a comparison of the receptivity spectra for different sampling locations was made for the finite spherical and planar disturbances respectively. The receptivity spectra for Case B1 and Case B2 at several sampling locations are presented in Fig. 28, while results for Cases B3 and B4 are omitted due to their similarity. The sampling locations were chosen to be the branch I neutral stability point $x_{brI}$, the branch II neutral stability point $x_{brII}$, and an intermediate location defined at $x_{sample} = 1.3 * x_{brI}$ for each discrete frequency. These points were chosen to ensure the sampling location remained within the unstable second mode region. The branch I sampling point compares directly to conventional receptivity results reported by Balakumar and Chou[21], Kara et al.[22], Zhong and Ma[18], and Huang and Zhong[26] as the normalization factor in this case is simply 1. Huang and Zhong stated that the total acoustic response at the branch I neutral point is likely to be contaminated by the multimodal content of the disturbance. This may make it difficult to apply the receptivity results for general transition studies in which only particular instability modes are of interest. However, for Cases B1 through B4, Fig. 28 shows that the second mode is dominant at all of the sampling points. While the branch I sampling case does show significantly more oscillations indicative of multimodal disturbances[26], the general shape and magnitude of the receptivity spectrum is in line with the other sampling locations.

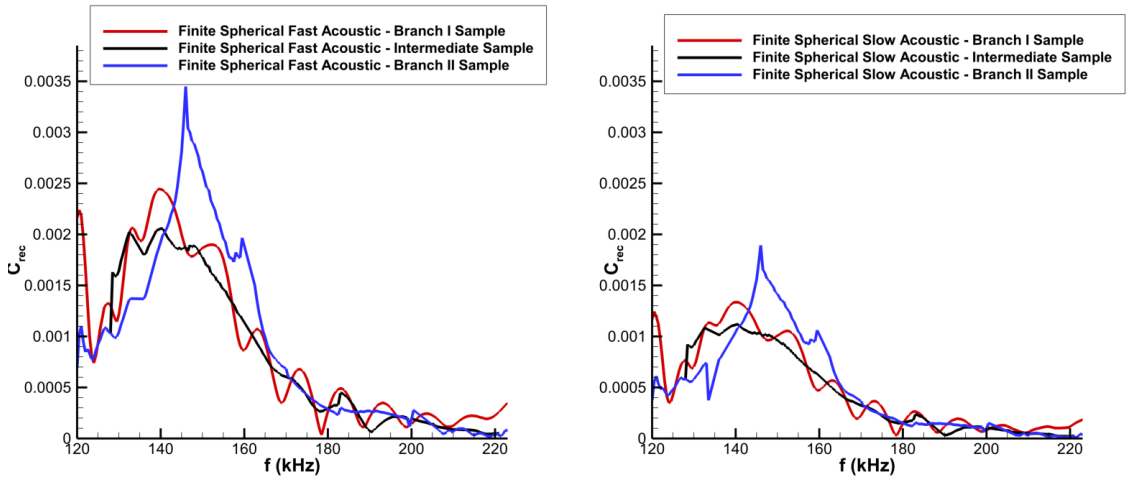


(a) (b)

**Fig. 28 Receptivity coefficients at different sampling locations for (a) Case B1 (b) Case B2.**

The branch II sampling location spikes near 140 kHz to 150 kHz, which correlates to the most amplified frequencies at the end of the computed domain. This spike may be due to the influence of the initial broadband disturbance and the

resulting broadband boundary layer disturbances that it excites. The complex perturbation environment is partially observed previously in the somewhat oscillatory DNS phase speed and growth rate results in Figs. 14-17. While general results indicate that the perturbations are strongly dominated by the second mode, variations originating from the complex response to broadband forcing can cause slight inconsistencies between the LST and DNS results across the total disturbance frequency spectra.

Fig. 29 presents the same data for the planar fast and slow acoustic freestream pulses in Case B5 and Case B6. Again, the results for the temperature and vorticity pulses in Cases B7 and B8 are omitted due to their similarity to Case B6. The receptivity coefficient spectra for Case B5 in Fig. 29a differ significantly from the finite spherical pulse cases, while the results in Fig. 29b for Case B6 are similar to those in Fig. 28 for cases B1 and B2. The magnitudes of the receptivity coefficients for the planar cases are also much higher. This is because planar disturbances generate significantly stronger boundary layer perturbations relative to the initial freestream disturbance amplitudes, as a result of their continuous forcing. The Fourier decomposition results presented in this study also do not account for the differences in wavenumber distributions between the finite spherical pulses and the semi-infinite planar pulses.

Case B6 seems to very readily excite both second mode and additional low frequency disturbances attributed to noise. The low frequency disturbances in particular are observed to be excited much more strongly than in the finite pulse cases. This can also be seen in the FFT contours shown in Fig. 22 where again the low frequency forcing generated by the planar pulse is observably much more present throughout the domain. The branch I sampling location results overpredicts the low frequency response compared to the other sampling locations, indicating that modal decomposition is necessary to capture the behaviors of the second mode. On the other hand, the intermediate and branch II sampling locations show very similar results, peaking at frequencies between 125 and 145 kHz. These results match well with the LST prediction, indicating that the second mode can be easily isolated using Huang and Zhong's method in this case.

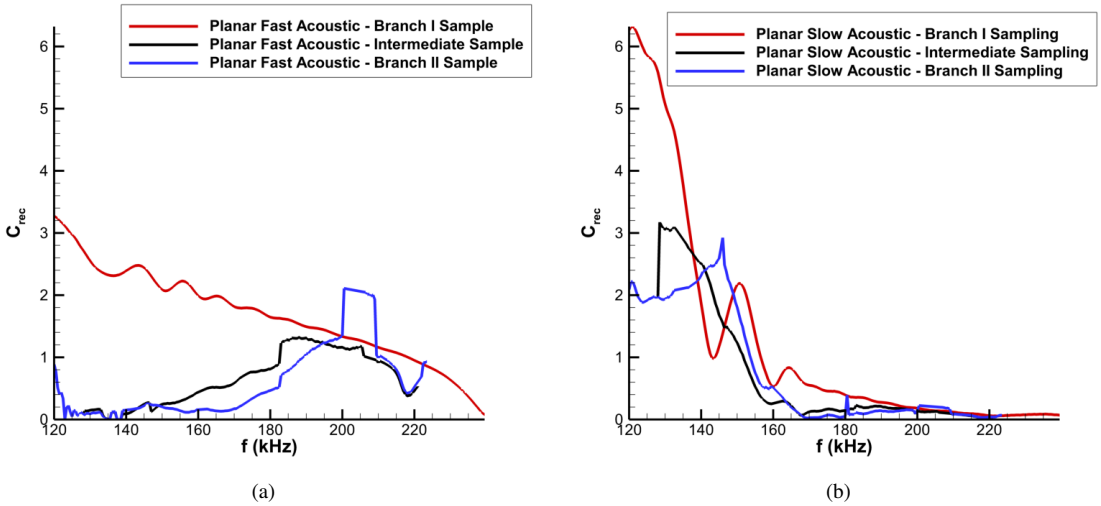


(a) (b)

**Fig. 29 Receptivity coefficients at different sampling locations for (a) Case B5 and (b) Case B6.**

The receptivity spectra for Case B5 in Fig. 29a differ significantly from Cases B1, B2, and B6. The branch I sampling location produces a continuous broadband receptivity coefficient distribution, similar to the initial pulse. This indicates that the broadband forcing excited by the planar fast acoustic pulse is strong enough to mask the initial second mode instability at the branch I neutral point, and that the planar fast acoustic pulse excites a very broad range of frequencies in comparison to all the other cases. The resulting combined disturbances at this location result in perturbation amplitudes far larger than those expected of the pure second mode. The other sampling locations also show that the receptivity coefficients are highest near 200 kHz, contrary to the finite spherical cases and LST results. Looking again at Fig. 22a it can be seen that an additional band of amplified disturbances can be found at these frequencies that is attributed to the strong surface forcing generated by the shock-disturbance interaction seen in Fig. 19. While significant second mode amplification is observed in all of the cases, Case B5 demonstrates that sufficiently noisy environments of fast acoustic disturbances can excite significant boundary layer disturbances not associated with the second mode for this geometry. This can potentially account for the somewhat weak association between the second mode and the

transition for this case that Marineau et al. observed [36].

The total receptivity spectra for the finite spherical cases (B1-B4) are shown in Fig. 30a and for the planar cases (B5-B8) in Fig. 30b at the intermediate sampling location. For the finite spherical pulses, it was found that the receptivity response was strongest for the fast acoustic, temperature, slow acoustic, and vorticity disturbances in that order. For the planar pulses the strongest second mode receptivity response was observed for the slow acoustic disturbance, followed by the temperature, vorticity, and fast acoustic pulses, though the planar fast acoustic pulse excited significant broadband waves in the boundary layer that weren't associated with the second mode as well.

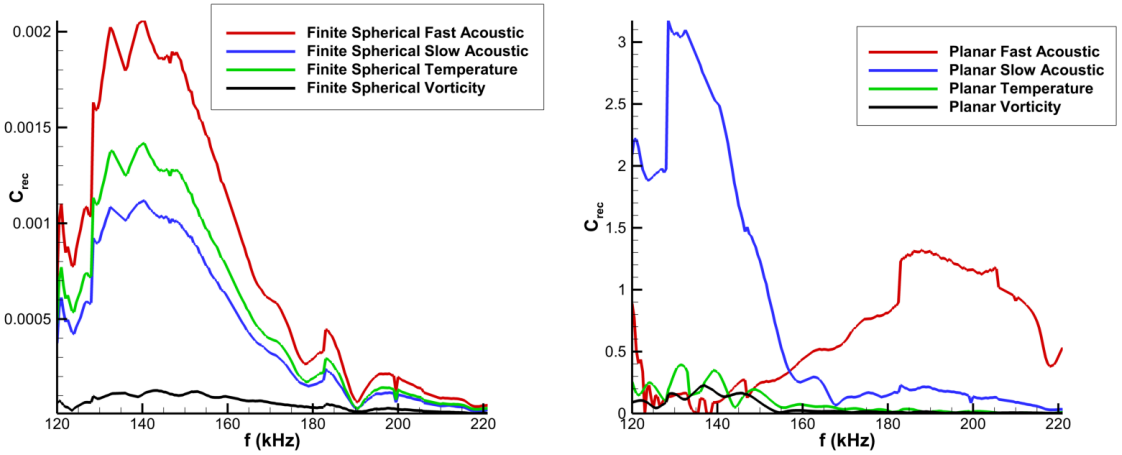


(a) (b)

**Fig. 30 Receptivity coefficient spectra for (a) Cases B1-B4 and (b) Cases B5-B8.**

### B. Disturbance Phase Angle Spectra

The phase angle spectra for the disturbance cases was also extracted from the unsteady DNS. With the data from the receptivity coefficient spectra and the phase angle spectra, the total initial receptivity response to an arbitrary axisymmetric freestream disturbance can be reconstructed[9, 23]. These initial disturbances can then be used as inputs for more advanced transition predicted methods like Mack's amplitude method[33], Crouch's variable N-factor method[31], Marineau's iterative method[34], and Ustinov's implementation of the amplitude methods[35]. This data can also be used to reproduce arbitrary inlet conditions for downstream simulations studying phenomena such as nonlinear breakdown [23, 50]. The frequency spectra of the disturbance phase angles are depicted for each of the pulse cases in Fig. 31. In particular, Fig. 31a details the finite spherical cases B1-B4 while Fig. 31b presents the same results for the planar disturbance cases B5-B8 at a streamwise position of $s^* = 1.49$ m. The unstable second mode frequency band, located between 140-170 kHz at this point, can be identified by a distinct change in the slope of the phase angle spectra at these frequencies. Furthermore, the end of the dominant second mode frequency band is indicated clearly in all cases by a discontinuity in the slope near 170 kHz.

The profiles of the finite pulse cases in Fig. 31a and the planar cases in Fig. 31b are very similar, though the range of phase angles is smaller for the finite pulse cases. Since the disturbance pulse interacts with the meanflow only in the nose region of the cone, the finite pulse cases generate significantly less forcing waves. This results in a much less noisy boundary layer disturbance profile and a narrower band of phase angles for the finite pulse cases. Particularly strong agreements were observed for Cases B1, B2, and B3 in Fig. 31a and between Cases B7 and B8 in Fig. 31b. For a pure second mode boundary layer disturbance, all of the phase spectra lines would be expected to perfectly align. However, the shock-disturbance interactions that occur from the impinging freestream pulses are known to generate complex disturbance environments composed of a combination of acoustic, entropy, and vorticity waves[8]. The receptivity response of the meanflow and the bow shock to different freestream disturbances can result in differing incident phase angles for the forcing waves[9]. This variability of the initial forcing can account for the differences in the phase spectra observed in Fig. 31.

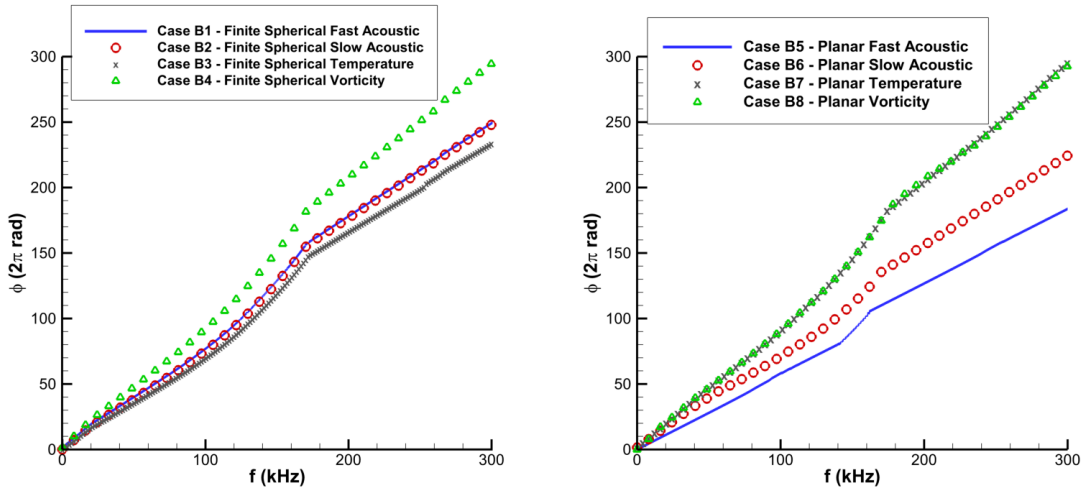


(a) (b)

**Fig. 31 Spectral phase angle plots for (a) finite spherical disturbances (Cases B1-B4) and (b) planar disturbances (Cases B5-B8) at $s^* = 1.49$ m.**

To illustrate the different effects the freestream disturbances have on the boundary layer forcing, the surface pressure time history at $s^* = 1.49$ m is presented in Fig. 32 for cases B1-B4. The primary second mode wavepackets are not displayed, as their general structure is very similar for these pulses. The surface pressure time history of the forcing closely follows the behaviors depicted in Fig. 31a, with Cases B1, B2, and B3 having very similar forcing disturbance profiles. This reflects a common receptivity response for these finite freestream pulse disturbances.

The surface pressure history for the forcing is similarly shown for cases B5-B8 in Fig. 33. Here, the forcing for Case B7 and Case B8 share significant structural similarities as expected from Fig. 31b. Contrary to what was observed for the finite spherical cases, the planar acoustic disturbances saw a sharp differentiation in the phase results between Case B5 and Case B6. A significant time lag is observed between the peak disturbance amplitudes between Cases B5, B6, and B7/B8 due to the different freestream propagation speeds of the pulses, which inherently introduces phase differences between these results.

The phase spectra at a selection of streamwise positions is shown for Case B1 in Fig. 34 with the dimensional frequency spectra in particular in Fig. 34a. The other finite pulse cases are omitted for concision. The disturbance phase angles are observed to steadily increase as the sampling position moves downstream. This is consistent with the formulation for positive phase speed calculations in Eq. 16 and Eq. 17. These spectra can also be plotted with respect to the non-dimensional circular frequency, which is defined by Eq. 20.

$$\omega = \frac{2\pi f_n L^*}{U_\infty} \tag{20}$$

where $L^*$ is a local boundary layer thickness length scale based on freestream parameters and the local streamwise position defined as:

$$L^* = \sqrt{\frac{\mu_\infty s^*}{\rho_\infty U_\infty}} \tag{21}$$

This nondimensionalization couples the results in Fig. 34b to both frequency and spatial location. The slope of the nondimensionalized spectra at each streamwise location is now also representative of the phase speeds of the disturbance. From Eq. 17 it is known that the phase speed scales inversely with the streamwise derivative of phase angle, which is related to the nondimensionalized phase spectra by $L^*$. As the sampling point moves further downstream the slopes of the spectra lines in both figures is observed to steadily increase. This behavior is consistent with the increasing dominance of the second mode instability, which in this case is the discrete mode F. As the sampling location moves downstream for Fig. 34b and Fig. 35b the phase spectra lines cluster closely together. This increasing coherence is further indication of the increasing dominance of the second mode disturbance downstream on the cone.

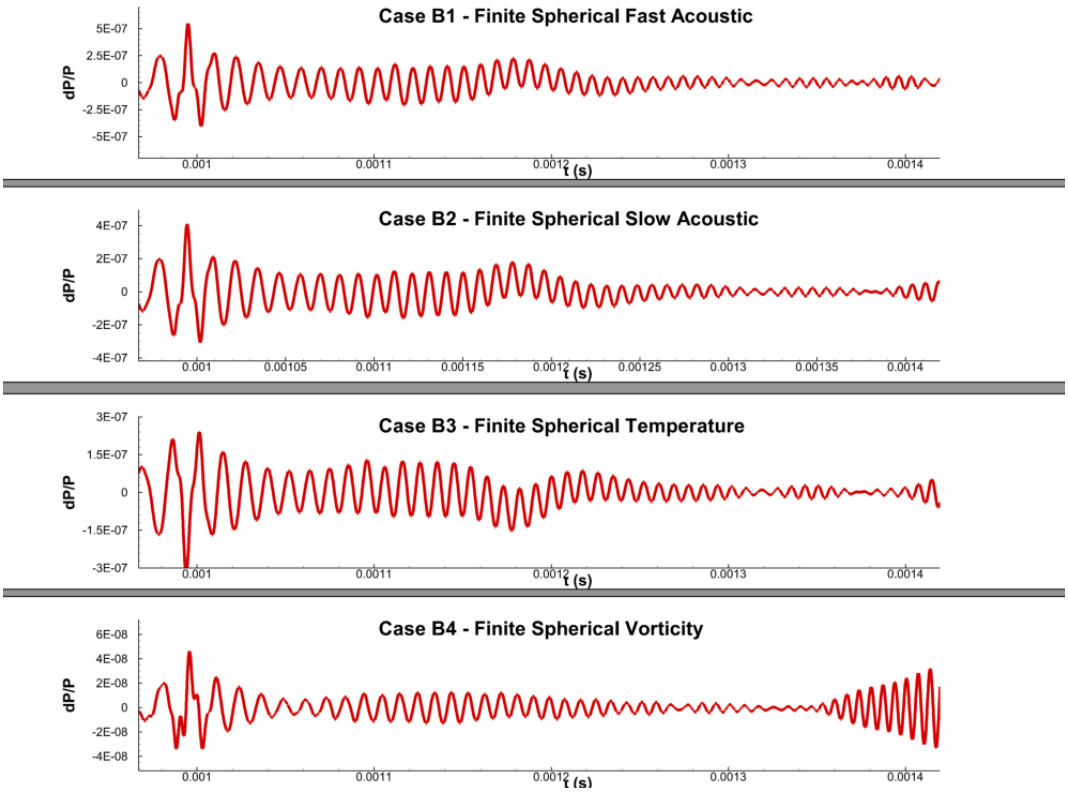


**Fig. 32 Time history of forcing disturbances at $s^*$ = 1.49 m for cases B1-B4 .**

Similar streamwise phase spectra results are presented for Case B5 in Fig. 35. Again, the dimensional spectral phase angle distributions for this case are presented in Fig. 35a while the non-dimensionalized phase angle spectra are shown in Fig. 35b. The results here follow closely with Case B1's, though the second mode frequencies demonstrate much stronger slope variations for Case B5. Distinct frequency bands in the phase slope were not observed for the amplified forcing frequencies that were identified in Section VII.B.

## IX. Discussion and Conclusion

The receptivity of a 7-degree half-angle, 9.525 mm nose radius cone at mach 10 to a variety of freestream disturbances with continuous, broadband frequency spectra was investigated in this study. Spectral receptivity coefficient amplitudes and phase angles were extracted for finite spherical and planar geometry pulses consisting of fast acoustic, slow acoustic, temperature, and vorticity disturbances. The base flow geometry and freestream conditions were based on Marinuea, et al.'s experiments[36] and the meanflow was converged using a high-order shock fitting method to solve the perfect gas Navier-Stokes equations (DNS). The stability of the meanflow was investigated using linear stability theory (LST) analysis and unsteady DNS. The pulses for unsteady DNS were modelled analytically in the freestream using Gaussian distributions to provide broadband frequency disturbances, and the shock interactions were simulated using the same high-order shock-fitting scheme as the steady DNS.

The LST analysis showed that boundary layer disturbances in a band of frequencies extending from approximately 118 kHz to 238 kHz experienced second mode growth. Furthermore, the discrete mode F emerging from the continuous fast acoustic spectrum was found to become the unstable second mode after synchronization. An entropy layer was observed beginning near the nose and the frustum, which eventually merged into the boundary layer at $s^*$ = 0.9881 m. Similar to Balakumar and Chou[21], LST and DNS did not predict peak second mode instability until after the entropy layer was swallowed. The N-factor in this study agrees well with Marineau et al.'s[36] PSE N-factor at the experimental transition location, with the results of this study predicting an N-factor of 1.7 vs Marineau et al.'s 1.6. The minor differences between these results is attributed to non-parallel effects that were ignored by the LST analysis utilized here.

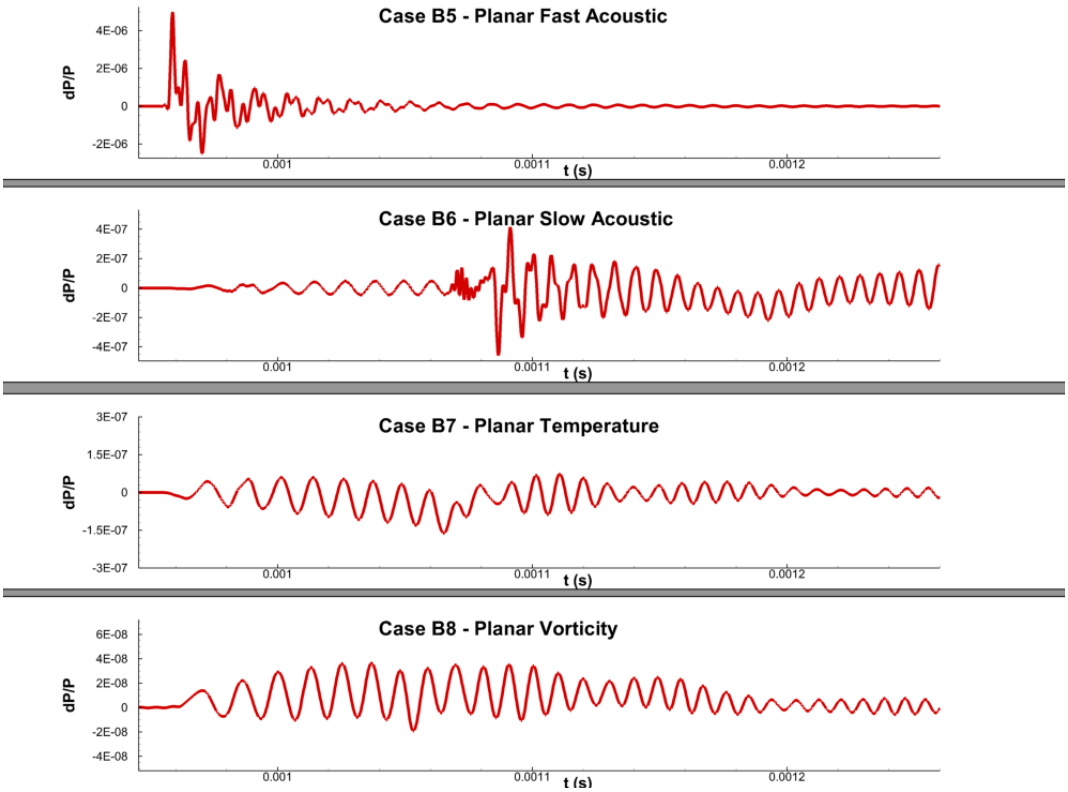


**Fig. 33 Time history of forcing disturbances at $s^* = 1.49$ m for cases B5-B8 .**

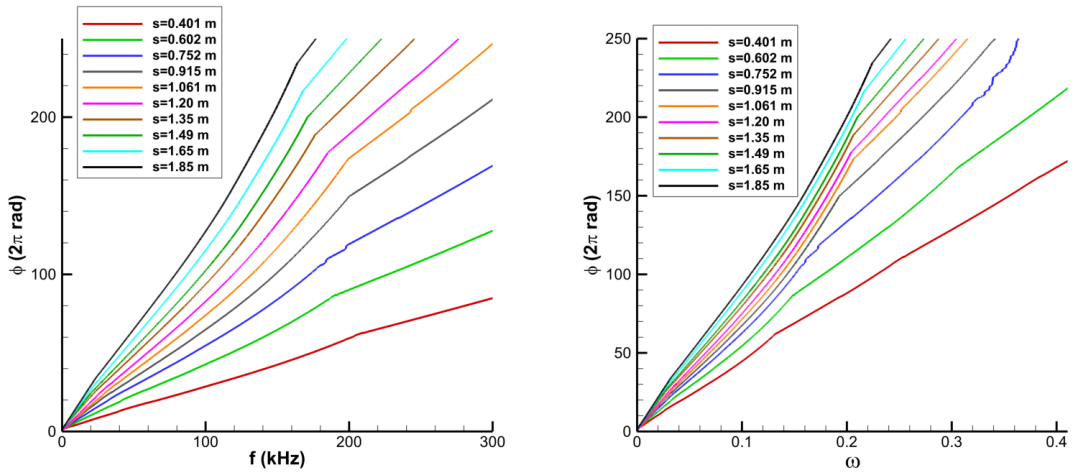


(a) (b)

**Fig. 34 Phase angle vs (a) dimensional frequency and (b) non-dimensional circular frequency at different streamwise locations for Case B1.**

The unsteady DNS simulations were decomposed into their frequency components using FFT which showed that all eight of the freestream pulse disturbances generated significant second mode amplification on the cone. The finite spherical pulse cases (B1-B4) were observed to generate very similar boundary layer disturbance profiles, with second mode disturbances beginning to dominate after $s^* = 1.2$ m. Due to their limited size, the finite pulses only interacted

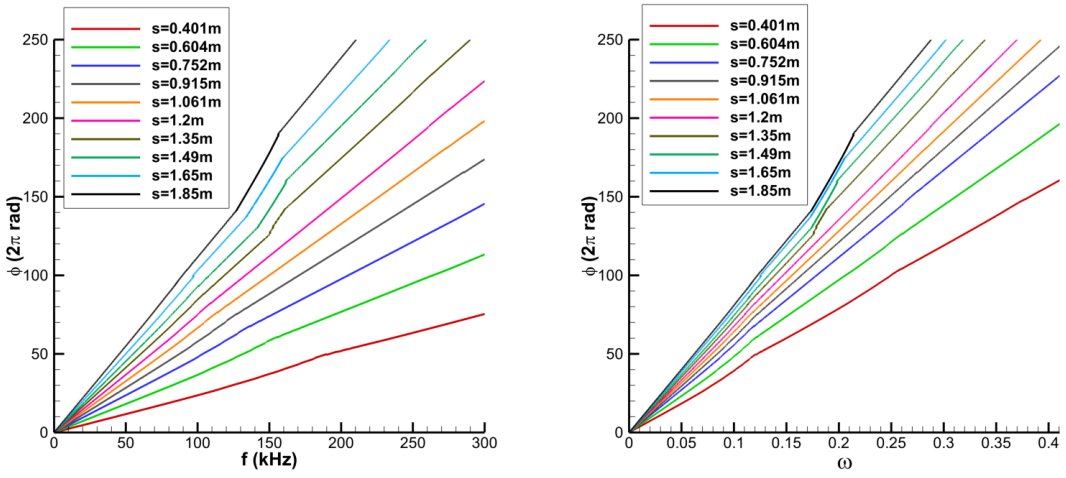


**Fig. 35 Phase angle vs (a) dimensional frequency and (b) non-dimensional circular frequency at different streamwise locations for Case B5.**

with the shock near the nose region of the cone. These isolated shock interactions allowed most of the initial broadband forcing to be damped out before second mode amplification began. In spite of the low freestream stagnation enthalpy, distinct supersonic modes were also observed for the finite pulse cases. These supersonic modes were identified by characteristic acoustic radiation emanating from the boundary layer disturbances, as shown in Fig. 10. However, the amplitude of the supersonic modes were significantly weaker than the second mode for most of the domain, and are unlikely to affect the primary transition observed experimentally. This does, however, further indicate that supersonic modes exist in a much wider range of flow conditions than previously thought, though their impact on transition still requires additional study. The unsteady DNS results were validated against LST and showed good agreement for all of the finite pulse cases. The strongest response amplitudes were observed in response to the finite fast acoustic (Case B1), temperature (Case B3), slow acoustic (Case B2), and vorticity (Case B4) pulses in that order.

The planar pulse disturbance cases (B5-B8) were also shown to readily excite the second mode disturbance and demonstrated good agreement against the 150 kHz disturbance results generated from LST. Stronger low frequency forcing was observed throughout, which was caused by the continuous introduction of new forcing waves across the domain from the interactions of the planar pulses and the bow shock. The additional forcing from the planar disturbances also resulted in broadened second mode frequency bands for the planar slow acoustic (Case B5), temperature (Case B7), and vorticity (Case B8) pulse cases. The receptivity response of the planar fast acoustic pulse (Case B5) differed greatly from the finite pulses and the other planar pulse cases. Additional bands of both lower and higher frequency disturbances were amplified along with the second mode in the streamwise direction. It was found that the planar fast acoustic pulse generated forcing waves at the shock-disturbance front that strongly excited these other disturbance frequencies directly in the boundary layer. This forcing was observed in the surface pressure time history as additional high-amplitude perturbations outside of the second mode wavepacket. It was found that these forcing waves greatly dominated over the second mode disturbance until approximately $s^* = 1.5$ m for Case B5. In terms of the second mode disturbance amplitudes, Case B6 experienced the strongest response followed by Case B7, Case B8, and finally Case B5. While Case B5 excited the smallest second mode amplitudes, the flow was shown to be much more receptive to broadband disturbance frequencies.

The receptivity coefficients for the second mode disturbances for the eight disturbance cases were calculated by rescaling unsteady DNS pressure perturbation data with the LST N-factors. This method specifically extracts the initial second mode amplitudes at the branch I neutral point from the unsteady DNS data for second mode dominated flows. Different sampling locations for the unsteady data were used to demonstrate the necessity of modal decomposition. It was found for the finite pulse cases that the forcing waves were sufficiently damped enough that the flow field was almost entirely dominated by the second mode, and that modal decomposition was not necessary. The planar pulse cases demonstrated much stronger forcing, with low frequency disturbances overshadowing the second mode in Cases

B6-B8 without modal decomposition. Case B5 saw a very broadband receptivity spectrum indicating a wide variety of amplified disturbance frequencies. The simple modal decomposition used in this study was found to be insufficient for this noisier case and may necessitate the use of more advanced modal decomposition techniques like biorthogonal decomposition[42, 43]. This is due in large part to the fact that the primary second mode disturbance was not found to dominate for Case B5 throughout the computational domain. Disturbance phase angle spectra were also extracted from the unsteady DNS data and were found to closely follow expected trends for mode F dominated flows. Observed differences in the phase spectra between the pulses can be attributed to the different forcing responses inherent to each freestream disturbance type.

Using the receptivity and phase spectra found in this study, it is possible to reconstruct the receptivity response of the meanflow to arbitrary axisymmetric disturbances [9, 23]. This can be directly used in the development and application of more advanced transition estimation procedures such as Crouch's[31] variable N-factor method or Mack's amplitude method[33] in order to improve the accuracy of transition predictions. However, additional non-axisymmetric disturbances must be considered in order to further generalize the receptivity response of the studied meanflow to a wider ranger of potential experimental and flight conditions. This requires the simulation and study of three-dimensional broadband disturbances. The application of more advanced multimode decomposition techniques may also be necessary to isolate disturbance modes of interest, as the methodology used here may not be able to isolate the second mode response in significantly noisy boundary layers.



## Acknowledgments

This research was partially supported by the Air Force Office of Scientific Research (AFOSR) under AFOSR Grant #FA9550-19-1-0206, monitored by Dr. Ivett Leyva, and by Office of Naval Research (ONR) Grant #N00014-17-1-2343, monitored by Dr. Eric Marineau. Primary computational resources were provided by Extreme Science and Engineering Discovery Environment (XSEDE) through the Texas Advanced Computing Center (TACC) and the San Diego Supercomputer Center (SDSC) under grant number TG-ASC090076, supported in part by the National Science Foundation (NSF). Additional computational support was provided by the Department of Defense High Performance Computing Modernization Program (DoD HPCMP) through project AFOSR40702004. The views and conclusions contained herein are those of the authors and should not be interpreted as necessarily representing the official policies or endorsements, either expressed or implied, of the U.S. Air Force Office of Scientific Research, Office of Naval Research, XSEDE, or the U.S. Government.

## References

[1] Fedorov, A., "Transition and Stability of High-Speed Boundary Layers," *Annual Review of Fluid Mechanics*, Vol. 43, 2011, pp. 79–95. https://doi.org/10.1146/annurev-fluid-122109-160750.

[2] Reshotko, E., "Hypersonic Stability and Transition," *Hypersonic flows for reentry problems*, Vol. 1, No. A93-42576 17-02, 1991, pp. 18–34.

[3] Zhong, X., and Wang, X., "Direct Numerical Simulation on the Receptivity, Instability, and Transition of Hypersonic Boundary Layers," *Annual Review of Fluid Mechanics*, Vol. 44, 2012, pp. 527–561. https://doi.org/10.1146/annurev-fluid-120710-101208.

[4] Ma, Y., and Zhong, X., "Receptivity of a Supersonic Boundary Layer over a Flat Plate. Part 3. Effects of Different Types of Free-stream Disturbances," *Journal of Fluid Mechanics*, Vol. 532, 2005, pp. 63–109. https://doi.org/10.1017/S0022112005003836.

[5] Mack, L. M., "Boundary layer stability theory," Tech. Rep. 900-277, JPL Report, 1969.

[6] Schneider, S., "Effects of High-Speed Tunnel Noise on Laminar-Turbulent Transition," *Journal of Spacecraft and Rockets*, Vol. 38, 2001, p. 323–333. https://doi.org/10.2514/2.3705.

[7] Kovasznay, L. S. G., "Turbulence in Supersonic Flow," *Journal of the Aeronautical Sciences*, Vol. 20, No. 10, 1953, pp. 657–682. https://doi.org/10.2514/8.2793.

[8] McKenzie, J. F., and Westphal, K. O., "Interaction of Linear Waves with Oblique Shock Waves," *Physics of Fluids*, Vol. 11, No. 11, 1968, pp. 2350–2362. https://doi.org/10.1063/1.1691825.

[9] Huang, Y., and Zhong, X., "Numerical Study of Hypersonic Boundary-Layer Receptivity and Stability with Freestream Hotspot Perturbations," *AIAA Journal*, Vol. 52, No. 12, 2014, pp. 2652–2672. https://doi.org/10.2514/1.J052657.

[10] Balakumar, P., and Malik, M., "Discrete modes and continuous spectra in supersonic boundary layers," *Journal of Fluid Mechanics*, Vol. 239, 1992, pp. 631–656. https://doi.org/10.1017/S0022112092004555.

[11] Ma, Y., and Zhong, X., "Receptivity of a supersonic boundary layer over a flat plate. Part 1. Wave structures and interactions," *Journal of Fluid Mechanics*, Vol. 488, 2003, pp. 31–78. https://doi.org/10.1017/S0022112003004786.

[12] Ma, Y., and Zhong, X., "Receptivity of a supersonic boundary layer over a flat plate. Part 2. Receptivity to freestream sound," *Journal of Fluid Mechanics*, Vol. 488, 2003, pp. 79–121. https://doi.org/10.1017/S0022112003004798.

[13] Malik, M., and Balakumar, P., "Receptivity of Supersonic Boundary Layers to Acoustic Disturbances," *35th AIAA Fluid Dynamics Conference and Exhibit*, 2005. https://doi.org/10.2514/6.2005-5027.

[14] Fedorov, A. V., "Receptivity of a High-Speed Boundary Layer to Acoustic Disturbances," *Journal of Fluid Mechanics*, Vol. 491, 2003, pp. 101–129. https://doi.org/10.1017/S0022112003005263.

[15] Fedorov, A. V., Ryzhov, A. A., Soudakov, V. G., and Utyuzhnikov, S. V., "Receptivity of a high-speed boundary layer to temperature spottiness," *Journal of Fluid Mechanics*, Vol. 722, 2013, p. 533–553. https://doi.org/10.1017/jfm.2013.111.

[16] Mack, L. M., "Boundary Layer Linear Stability Theory," Tech. rep., AGARD report No. 709, 1984.

[17] Fedorov, A., and Tumin, A., "High-Speed Boundary-Layer Instability: Old Terminology and a New Framework," *AIAA Journal*, Vol. 49, No. 8, 2011, pp. 1647–1657. https://doi.org/10.2514/1.J050835.

[18] Zhong, X., and Ma, Y., "Boundary-Layer Receptivity of Mach 7.99 Flow over a Blunt Cone to Free-Stream Acoustic Waves," *Journal of Fluid Mechanics*, Vol. 556, 2006, pp. 55–103. https://doi.org/10.1017/S0022112006009293.

[19] Balakumar, P., and Kegerise, M., "Receptivity of Hypersonic Boundary Layers over Straight and Flared Cones," *48th AIAA Aerospace Sciences Meeting Including the New Horizons Forum and Aerospace Exposition*, 2010. https://doi.org/10.2514/6.2010-1065.

[20] Balakumar, P., and Kegerise, M., "Receptivity of Hypersonic Boundary Layers to Acoustic and Vortical Disturbances," *49th AIAA Aerospace Sciences Meeting including the New Horizons Forum and Aerospace Exposition*, 2011. https://doi.org/10.2514/6.2011-371.

[21] Balakumar, P., and Chou, A., "Transition Prediction in Hypersonic Boundary Layers Using Receptivity and Freestream Spectra," *AIAA Journal*, Vol. 56, No. 1, 2018, pp. 2593–2606. https://doi.org/10.2514/1.J056040.

[22] Kara, K., Balakumar, P., and Kandil, O., "Effects of Nose Bluntness on Hypersonic Boundary-Layer Receptivity and Stability over Cones," *AIAA Journal*, Vol. 55, No. 12, 2011, pp. 2593–2606. https://doi.org/10.2514/1.J050032.

[23] Lei, J., and Zhong, X., "Numerical Simulation of Freestream Waves Receptivity and Breakdown in Mach 6 Flow over Cone," *43rd Fluid Dynamics Conference*, 2013. https://doi.org/10.2514/6.2013-2741.

[24] Reshotko, E., and Tumin, A., "Role of Transient Growth in Roughness-Induced Transition," *AIAA Journal*, Vol. 42, No. 4, 2004, pp. 766–774. https://doi.org/10.2514/1.9558.

[25] Lei, J., and Zhong, X., "Linear Stability Analysis of Nose Bluntness Effects on Hypersonic Boundary Layer Transition," *Journal of Spacecraft and Rockets*, Vol. 49, No. 1, 2012, pp. 24–37. https://doi.org/10.2514/1.52616.

[26] Huang, Y., "Numerical Study of Hypersonic Boundary-Layer Receptivity and Stability with Freestream Hotspot Perturbations," Ph.D. thesis, University of California, Los Angeles, 2016.

[27] Wheaton, B., Juliano, T., Berridge, D., Chou, A., Gilbert, P., Casper, K., Steen, L., and Schneider, S., "Instability and Transition Measurements in the Mach-6 Quiet Tunnel," *39th AIAA Fluid Dynamics Conference*, 2009. https://doi.org/10.2514/6.2009-3559.

[28] Chou, A., "Characterization of Laser-Generated Perturbations and Instability Measurements on a Flared Cone," Master's thesis, Purdue University, West Lafayette, IN, 2010.

[29] Chou, A., Wheaton, B., Ward, C., Gilbert, P., Steen, L., and Schneider, S., "Instability and Transition Reserach in a Mach-6 Quiet Tunnel," *49th AIAA Aerospace Sciences Meeting*, 2011. https://doi.org/10.2514/6.2011-283.

[30] Chang, C., Malik, M., Erlebacher, G., and Hussaini, M., "Compressible stability of growing boundary layers using parabolized stability equations," *22nd Fluid Dynamics, Plasma Dynamics and Lasers Conference*, 1991. https://doi.org/10.2514/6.1991-1636, URL https://arc.aiaa.org/doi/abs/10.2514/6.1991-1636.

[31] Crouch, J., and Ng, L., "Variable N-Factor Method for Transition Prediction in Three-Dimensional Boundary Layers," *AIAA Journal*, Vol. 38, No. 2, 2000. https://doi.org/10.2514/2.973.

[32] Reed, H. L., Saric, W. S., and Arnal, D., "Linear Stability Theory Applied to Boundary Layers," *Annual Review of Fluid Mechanics*, Vol. 28, No. 1, 1996, pp. 389–428. https://doi.org/10.1146/annurev.fl.28.010196.002133.

[33] Mack, L. M., "Transition Prediction and Linear Stability Theory," Tech. rep., AGARD CP-224, 1977.

[34] Marineau, E., "Prediction Methodology for Second-Mode dominated Boundary-Layer Transition in Wind Tunnels," *AIAA Journal*, Vol. 55, No. 2, 2017. https://doi.org/10.2514/1.J055061.

[35] Ustinov, M. V., "Amplitude method of prediction of laminar-turbulent transition on a swept-wing," *Fluid Dynamics*, Vol. 52, No. 1, 2017, pp. 71–87. https://doi.org/10.1134/S0015462817010070.

[36] Marineau, E., Moraru, C., Lewis, D., Norris, J., and Lafferty, J., "Mach 10 Boundary-Layer Transition Experiments on Sharp and Blunted Cones," *19th AIAA International Space Planes and Hypersonic Systems and Technologies Conference*, 2014. https://doi.org/10.2514/6.2014-3108.

[37] Zhong, X., "High-Order Finite-Difference Schemes for Numerical Simulation of Hypersonic Boundary-Layer Transition," *Journal of Computational Physics*, Vol. 144, No. 2, 1998, pp. 662–709. https://doi.org/10.1006/jcph.1998.6010.

[38] Williamson, J., "Low-Storage Runge-Kutta Schemes," *Journal of Computational Physics*, Vol. 35, No. 1, 1980, pp. 48–56. https://doi.org/10.1016/0021-9991(80)90033-9.

[39] Malik, M. R., "Numerical Methods for Hypersonic Boundary Layer Stability," *Journal of Computational Physics*, Vol. 86, 1990, pp. 376–413. https://doi.org/10.1016/0021-9991(90)90106-B.

[40] Aleksandrova, E., Novikov, A., Utyuzhnikov, S., and Fedorov, A., "Experimental Study of the Laminar-Turbulent Transition on a Blunt Cone," *Journal of Applied Mechanics and Technical Physics*, Vol. 55, No. 3, 2014, pp. 375–385. https://doi.org/10.1134/S0021894414030018.

[41] Zhong, X., "Leading-Edge Receptivity to Free Stream Disturbance Wave for Hypersonic Flow Over a Parabola," *Journal of Fluid Mechanics*, Vol. 441, 2001, pp. 315–367. https://doi.org/10.1017/S0022112001004918.

[42] Tumin, A., "Three-Dimensional Spatial Normal Modes in Compressible Boundary Layers," *Journal of Fluid Mechanics*, Vol. 586, 2007, pp. 295–322. https://doi.org/10.1017/S002211200700691X.

[43] Miselis, M., Huang, Y., and Zhong, X., "Modal Analysis of Receptivity Mechanisms for a Freestream Hot-Spot Perturbation on a Blunt Compression-Cone Boundary Layer," *46th AIAA Fluid Dynamics Conference*, 2016. https://doi.org/10.2514/6.2016-3345.

[44] Lei, J., and Zhong, X., "Linear Stability Analysis of Nose Bluntness Effects on Hypersonic Boundary Layer Transition," *48th AIAA Aerospace Sciences Meeting Including the New Horizons Forum and Aerospace Exposition*, 2010. https://doi.org/10.2514/6.2010-898.

[45] Knisely, C. P., and Zhong, X., "Significant Supersonic Modes and the Wall Temperature Effect in Hypersonic Boundary Layers," *AIAA Journal*, 2019. https://doi.org/10.2514/1.J057775.

[46] Knisely, C. P., and Zhong, X., "Sound radiation by supersonic unstable modes in hypersonic blunt cone boundary layers. I. Linear stability theory," *Physics of Fluids*, Vol. 31, No. 2, 2019, p. 024103. https://doi.org/10.1063/1.5055761.

[47] Knisely, C. P., and X., Z., "Sound radiation by supersonic unstable modes in hypersonic blunt cone boundary layers. II. Direct numerical simulation," *Physics of Fluids*, Vol. 31, No. 2, 2019, p. 024104. https://doi.org/10.1063/1.5077007.

[48] Mortensen, C. H., "Toward an understanding of supersonic modes in boundary-layer transition for hypersonic flow over blunt cones," *Journal of Fluid Mechanics*, Vol. 846, 2018, p. 789–814. https://doi.org/10.1017/jfm.2018.246.

[49] Mack, L., "Review of Linear Compressible Stability Theory," *Stability of Time Dependent and Spatially Varying Flows*, edited by D. Dwoyer and M. Hussaini, Springer-Verlag, New York, 1985.

[50] Sivasubramanian, J., and Fasel, H. F., "Direct numerical simulation of transition in a sharp cone boundary layer at Mach 6: fundamental breakdown," *Journal of Fluid Mechanics*, Vol. 768, 2015, p. 175–218. https://doi.org/10.1017/jfm.2014.678.